J. Fluid Mech. (1995), vol. 299, pp. 333–366

Particle motion in the stagnation zone of an impinging air jet

By STEVEN L. ANDERSON AND ELLEN K. LONGMIRE

Department of Aerospace Engineering and Mechanics, University of Minnesota, 110 Union Street S.E., Minneapolis, MN 55455, USA

(Received 19 August 1994 and in revised form 18 May 1995)

This study investigated particle behaviour in the stagnation zone of natural and forced round impinging air jets using flow visualization, image analysis, and particle image velocimetry. The jet Reynolds number was 21000, and the nozzle to plate spacing was five diameters. Small mass loadings of glass beads with inertial time constants τ_p of 1.7 and 7 ms were examined. The Stokes number associated with the mean flow $St_m = \tau_p U_0/D$ ranged from 0.6 to 2.4, and the Stokes number associated with vortices in the forced flow $St' = \tau_p f$ ranged from 0.3 to 1.25 where f is the vortex passage frequency. Particle velocities near the wall deviated strongly from fluid velocities, resulting in rebound and non-Stokesian effects (i.e. significant particle Reynolds numbers Re_p). The deceleration associated with rebounding caused long particle residence times in the stagnation zone and significant increases in particle number density above the plate. Rebound height and the height of the region of particle accumulation were well correlated and increased with St_m. Particles associated with lower St_m were accelerated in the radial direction more quickly, not only because of their decreased inertia, but also because of the larger fluid velocties encountered. Shear layer vortices produced spatial variations in particle concentration in the free jet which caused number density near the plate to fluctuate with time. The vortices had little effect on particle motion near the stagnation point, however. Only particles in the vicinity of vortex cores felt the influence of the vortex-induced velocity field. Hence, particle motion in the stagnation zone was most dependent on the mean flow (and thus St_m).

1. Introduction

In the past few years, much effort has been spent trying to understand and model turbulent gaseous flows containing discrete particles. When the particles do not follow the fluid phase exactly, a set of coupled nonlinear differential equations is required to describe the motion of the two phases. Since these equations cannot be solved analytically, good engineering models for particle-laden flows are highly desirable. To design efficient flow devices, manufacturers often require an understanding of typical instantaneous conditions within the flow, including particle distributions and velocities. For example, the transitory distribution and flow pattern of reactants in a pulverized-coal combustor greatly affects the parameters of the reaction. Fuel particles that are concentrated in dense clusters experience a much richer burning environment than particles which are evenly dispersed. If these clusters occur near the combustor walls, they must affect local heat transfer characteristics. Also, particle-laden flow around turbine blades induces wear and erosion on the blade surfaces.

Thus it becomes important in the blade design process to consider the frequency and location of particle–blade collisions with respect to the local gas flow structure.

In both of these examples, the gas phase of the flow is highly complex, containing eddies encompassing a wide range of scales. The equation of motion for an individual particle in this type of flow is thus correspondingly complex. Therefore, most of the recent experimental work on these flows has focused on examining the influence of simple individual effects which dominate. In particular, a number of recent experimental and numerical studies have shown that particle motion depends strongly on the relationship between particle inertia and the strength of local fluid eddies. Particle inertia has been quantified using an aerodynamic response time, τ_p:

$$\tau_p = \frac{\rho_p d_p^2}{18\mu} \tag{1.1}$$

where ρ_p is the particle density, d_p is the particle diameter, and μ is the fluid viscosity. This definition is based on flow in the Stokes regime and assumes that the fluid density is much less than the particle density. A corresponding fluid time scale is usually associated with the vorticity-bearing eddies in the flow. In free shear flows, for example, the fluid time scale is often based on the length scale (L) and propagation velocity (U_v) of the coherent vortices formed due to Kelvin–Helmholtz instabilities:

$$\tau_f = \frac{L}{U_v}. \tag{1.2}$$

The ratio of particle to fluid time scales is then defined as the Stokes number St (Crowe, Gore & Troutt 1985). Recent investigations that have examined Stokes number effects include studies on free shear flows, jets, and homogeneous turbulence. Collectively, the studies have shown two phenomena that are highly dependent on Stokes number: particle dispersion and particle concentration.

Experiments and computations on free shear layers and round jets have shown that particle dispersion is greatest for St on the order of unity (Kamalu *et al.* 1988, 1989; Wen *et al.* 1992; Hishida, Ando & Maeda 1992; Chein & Chung 1987; Chung & Troutt 1988; Longmire & Eaton 1992). In this range of St, particle motion becomes coupled with the motion of the large vortices present, and particles can be dispersed further than fluid elements. The effect of vortices on particle dispersion decreases as St increases, but continues to be strong for St up to 4 or 5. In the numerical study of Chein & Chung, particles were dispersed the furthest from the high-speed side of the mixing layer during vortex pairing. Thus, particle location with respect to large eddies is also important.

Numerical studies of particles in homogeneous turbulence have shown that St has a strong effect on instantaneous particle distribution. Asymptotic analysis by Maxey (1987) revealed that the divergence of the particle velocity field was negative in regions of high strain rate and positive in regions of high vorticity. Therefore, particle inertia can produce a bias in particle motion toward straining regions. Squires & Eaton (1991) used direct numerical simulation to show that particles of $St = 0.15$ yielded the greatest particle concentrations in regions of high strain rate. Maximum concentration levels in these regions were greater than 25 times the mean. Here, the Stokes number was based on the turbulence intensity and the wavenumber corresponding to the maximum in the energy spectrum. In a similar study, Wang & Maxey (1993) found that the Kolmogorov scale, corresponding to the smallest eddies in the flow, yielded the best collapse of the data in determining non-uniformity of particle concentration.

Zones of particle concentration have also been identified in free shear flows and jets. Lazaro & Lasheras (1989, 1992*a*, *b*) and Wen *et al.* (1992) found that for $St \approx 1$, particles released across a shear layer form highly concentrated streaks which align with the braid regions between successive vortices (i.e. areas of high strain rate). In a numerical study, Martin & Meiburg (1994) found pairs of streaks for larger St, indicating overshoot and oscillatory motion near the saddle points. In an axisymmetric jet, Longmire & Eaton (1992) showed that particles collect in the straining regions downstream of each vortex ring, with the greatest accumulations for the lowest Stokes number examined $St = 7.5$. In all of the above studies, particle number densities within vortex core regions or regions of high vorticity were lower than the mean when St was on the order of 1.

A current research goal is to go beyond the simplest Stokes number characterization of particle-laden flows. In an inviscid vortex model of a particle-laden jet, Hansell, Kennedy & Kollmann (1992) showed that at high particle Reynolds numbers, Basset, virtual mass, and fluid forces become significant in affecting particle dispersion. In particular, these forces tended to increase particle dispersion over that caused by drag forces alone. Ishima, Hishida & Maeda (1993) extended the work on particle-laden shear layers to account for the effect of particle residence time. They concluded that when slip velocities are large, particle dispersion is reduced. Therefore, the characteristic fluid time scale should depend on the interaction time between particles and large-scale eddies, and particles with longer residence times should experience greater dispersion. Longmire & Eaton (1994) postulated the same effect in their free jet experiments where nearly matching particle and vortex propagation velocities allowed for long residence times.

Few previous studies have examined the interaction of particles and coherent structures in wall-bounded flows. Existing results are limited to straight-walled boundary layer or channel flows where particle–structure interactions are difficult to characterize (Rashidi, Hetsroni & Banerjee 1990; Pedinotti, Mariotti & Banerjee 1992). The current study attempts to investigate particle motion in the stagnation region of an impinging jet where strong decelerations and accelerations as well as particle rebound are emphasized. The presence of a solid boundary, which adds complexity to the flow, must be important in practical situations and hence in models for realistic flows. Since heavy particles cannot adjust immediately to accelerations in the gas phase, particle residence time is likely to be an important parameter. Also, instantaneous drag forces and rebounding should be significant.

The structure and behaviour of single-phase impinging jets have been studied by Didden & Ho (1985) and Landreth & Adrian (1990). Both studies identified the existence of large primary vortices in the free jet, which expanded radially as they approached the impingement surface. The primary structures induced the formation of secondary, counter-rotating vortices, indicating local occurrences of boundary layer separation.

A few recent experiments have examined time-averaged behaviour in particle-laden impinging jets (Shimizu, Echigo & Hasegawa 1979; Kurosaki *et al.* 1986; Yoshida, Suenaga & Echigo 1990). In each study, particles and air exited a long tube and impinged on a flat surface downstream. Kurosaki *et al.* (1986) postulated that heat transfer rates increase near the stagnation point owing to the disruption of the viscous sub-layer by impacting particles. To examine this idea, Yoshida *et al.* (1990) obtained LDA measurements of fluid and particle velocities near the impingement surface for a tube exit velocity of 15 m s^{-1} and glass beads with 50 μm diameter ($\tau_p \approx 20$ ms). The authors observed that particle rebound was significant and

that particle number density increased dramatically near the stagnation zone. For moderate particle loadings (10% of the mass flux), the turbulence intensity in the fluid phase increased significantly near the stagnation point. These studies did not include instantaneous flow visualization or field measurements, leaving the effect of flow structure on particle motion unknown.

Previous work thus gives us a good understanding of the instantaneous structure of single-phase impinging jets but not of particle-laden impinging jets. We do not know of any previous work regarding time-resolved behaviour of particles subject to strong deceleration and acceleration near a solid boundary. The current study attempts to determine how particle motion is affected by both the presence of the wall itself and coherent structures near the wall. Some questions to be answered are: How does particle motion near the wall differ from that in free shear layers? Do Stokes numbers indicating preferential concentration differ from those in free shear flows? Why or why not? How do coherent structures affect particle motion near the wall? In answering these questions, we hope to point out aspects of models in wall-bounded flows which should be modified compared with those in homogeneous or free shear flows.

The impinging jet flow chosen for this investigation allowed for a quasi-axisymmetric flow in the stagnation region with coherent structures large enough to be observed easily. The jet could be forced to regulate the structure spacing. Particles of two time-constant ranges were added to the jet to examine inertial effects. Particle mass loadings were kept low (less that 5%) in order to minimize particle–particle interactions and any modification of the fluid phase. In addition, the impingement surface was placed far enough downstream that particle and fluid mean velocities matched as the flow approached the stagnation zone. Thus, particle residence times in the initially decelerating stagnation zone could be quantified. Two Stokes numbers were used to characterize the flow:

$$St_m = \frac{\tau_p U_0}{D} \quad \text{and} \quad St' = \tau_p f, \tag{1.3}$$

where D, U_0, and f are the jet exit diameter, velocity, and vortex passage frequency respectively. The first number characterizes the relationship between the mean flow and particles, while the second characterizes the relationship between the fluctuating flow and particles.

2. Facility

The flow facility was designed to produce an axisymmetric air jet with an initially thin shear layer and low core turbulence level. The particle feeding system was designed to yield a steady, controllable flow of particles which were reasonably well dispersed at the nozzle exit. Smoke seeding systems were included for both visualization and PIV purposes.

The flow system used for all experiments is shown in figure 1. The air flow was driven by a variable-speed centrifugal blower (Paxton model RM-80) electronically controlled by a transistor inverter (Toshiba model G2-2025). The flow, carried by a flexible hose, passed through a laminar flow meter, which consisted of a section of PVC pipe embedded with a piece of honeycomb flow straightener. A differential pressure transducer measured the pressure drop across the honeycomb, and the results were calibrated against Pitot tube measurements taken at the jet exit.

Downstream of the flow meter, particles were added by a variable-rate screw feeder

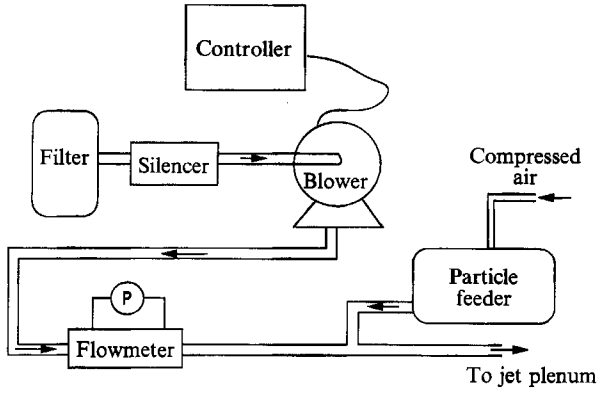

FIGURE 1. Schematic diagram of the flow path and particle feeder.

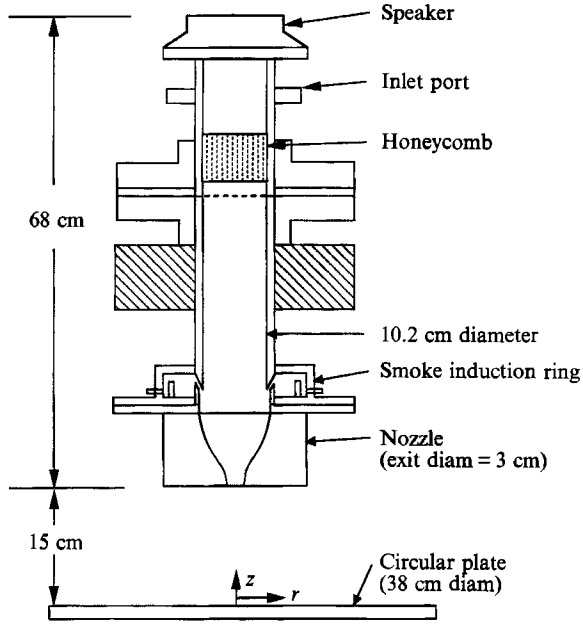

FIGURE 2. Jet facility and orientation to the impingement plate.

(Accu-rate 312). The agitated hopper was pressurized slightly to match conditions in the air-carrier hose. Particle feed rates were quite precise and controllable. The particles entered the flow through a connecting 'T', and the flow was subsequently split into two 1 inch diameter hoses which fed the jet.

A diagram of the jet is shown in figure 2. The main body of the jet was constructed of PVC pipe with 4 inch nominal inner diameter. The flow entered the plenum through two diametrically opposed inlet ports and subsequently passed through a honeycomb flow straightener to eliminate swirl and a screen to disperse particles. The inner surface of the plenum was coated with conductive paint and grounded in order to minimize static charging of the particles.

The flow accelerated through a smooth aluminium contraction attached to the bottom end of the plenum. The profile of the contraction was obtained by fitting a fifth-order polynomial to the end dimensions with the requirements that the slope

Particle group	T7	T2
ρ_p (kg m^{-3})	2500	340
d_p ([9pt]μm)	25–35	30–55
$\bar{d}_p$ ([9pt]μm)	30	40
τ_p (ms)	4.8–9.5	0.9–3.2
$\bar{\tau}_p$ (ms)	6.9	1.7
St_m	1.7–3.4	0.3–1.1
$\overline{St}_m$	2.4	0.6
St'	0.9–1.7	0.2–0.6
$\overline{St'}$	1.25	0.3

TABLE 1. Particle characteristics.

and curvature be zero at both ends. The nozzle exit diameter D was 3 cm, giving a contraction area ratio of 12.1:1. The entire jet was bracketed to a traverse with the jet oriented vertically downward. The impingement surface was a circular glass plate which rested upon an open metal frame, and the distance from the nozzle exit to the plate was fixed at 5 exit diameters. A large canvas tent enclosed the jet and glass plate in order to contain particles.

The jet was forced acoustically with a conventional audio speaker located at the upper end of the plenum. The signal sent to the speaker was a filtered and amplified sine wave generated by a Macintosh IIx computer. Forcing amplitudes were large enough to produce repeatable large-scale vortex rings in the shear layer which persisted down to the plate. A porous membrane was placed between the speaker and the plenum cavity to retard particle contamination of the speaker diaphragm.

For visualization of the fluid phase, smoke from a commercial fog generator (Rosco 1500) was fed into the flow by either of two methods: through two opposing ports in the upper plenum to mark the jet core; or through an induction ring just upstream of the nozzle to concentrate the smoke in the jet shear layer. The ring consisted of a cavity fed by four equally spaced inlet ports. The smoke entered the plenum boundary layer through an angled slit of 0.06 inch width. The fog machine was placed in a large steel drum which was pressurized slightly to match conditions in the plenum. The additional flow rate from the smoke system was accounted for in mass flow rate measurements.

The facility was qualified by measuring mean and r.m.s. velocity profiles of the jet near the nozzle exit with a single hot wire. A top-hat mean velocity profile was found with initial turbulence level of 0.4% in the unforced jet core and initial shear layer momentum thickness θ_m of 0.14 mm. Spectral analysis of measurements in the shear layer revealed an initial disturbance frequency f_o of 950 Hz corresponding to a Strouhal number based on θ_m of 0.013.

The solid phase of the flow consisted of two sets of spherical glass beads, referred to as T7 and T2 particles. Table 1 summarizes the characteristics of each group. A sample of T7 particles ($\tau_p = 6.9$ ms) was analysed for size distribution by a Coulter counter. The results showed that 95% of the mass fell between 25 and 37 μm. A microscope was used to determine the size distribution of T2 particles ($\tau_p = 1.7$ ms). Eighty percent of the particles fell within a diameter range of 35 and 45 μm, and 91% were between 30 and 55 μm. A very high percentage of the particles in each group were spherical.

3. Experimental techniques

3.1. *Flow visualization*

Instantaneous images of the gas and solid phases were obtained by illuminating the flow with a Nd:YAG pulsed laser (Continuum Surelite I). Normal operating frequency and pulse duration were 10 Hz and 5–6 ns respectively. The beam passed through a 1 m focal length spherical lens and a 12.7 mm cylindrical lens to form diverging, vertical light sheets aligned with the jet axis. The sheet thickness near the jet, which was approximately 0.5 mm, varied less than 0.1 mm over the field of view. The sheet height was large enough to illuminate the flow from the nozzle exit to the plate with little variation in light intensity.

For gas-phase visualizations, the fog generator produced an aerosol of fine droplets by vaporizing a glycerin-based fluid. The mean diameter of the droplets (1.2 μm) was measured by a Dantec phase Doppler anemometry system. For visualizations of the solid phase, low particle mass loadings were added to the gas phase. Mass loading was 3.4% for T7 particles and less than 1% for T2 particles. Therefore, disturbance to the gas phase was assumed negligible.

Light scattered perpendicular to the laser sheet was captured by a Nikon 8008s 35 mm camera fitted with a 105 mm micro lens. Kodak T-MAX 400 film was used for both gas and particle phases. A timing circuit was employed to externally control laser output and camera shutter opening to ensure that only one laser pulse was recorded in each frame. For forced studies, laser output was phase locked with the sine wave sent to the speaker. A 10 Hz square wave generated by the Macintosh computer was the reference wave form for the circuit.

Close-up photographs of particle trajectories were obtained by illuminating the stagnation zone with pulsed light sheets from an argon-ion laser. The continuous beam was acousto-optically modulated by a TTL-controlled Bragg cell. The modulation frequency and pulse duration were 10.5 kHz and 47 μs respectively. The beam passed through a 1 m focal length spherical lens and 50 mm and 300 mm focal length cylindrical lenses to form a 2.5 cm high, parallel sheet that sliced through the jet diameter immediately above the plate. For these visualizations, particle mass loading was less than 1%. The flow was photographed on TMAX 400 film with the same camera mentioned above. Each frame was exposed to a coded four-pulse sequence so that velocity magnitude and direction could be determined. Overall magnification was 0.675.

3.2. *Particle image velocimetry*

Instantaneous velocity fields of both gas and solid phases were obtained using particle image velocimetry (PIV). The illumination and acquisition setup is shown in figure 3. Two frequency-doubled, pulsed Nd:YAG lasers were mounted side-by-side on an optical bread board. The beam paths were combined with a set of mirrors and a polarization beam splitter. The initial polarization of the lasers was such that the on-axis beam was transmitted by the 'splitter' while the off-axis beam was reflected. The beams subsequently passed through a 1 m focal length spherical lens and a 50 mm focal length cylindrical lens to form vertical light sheets which intersected the jet axis near the stagnation zone. Laser output was on the order of 100 mJ per pulse, and the time delay Δt between pulses from the two lasers was 15.2 μs.

The flow was seeded independently with either smoke or glass particles. The smoke generator and particle feeder were adjusted so that particle number density was appropriate for the application of PIV (i.e. near 5 image pairs mm^{-2}). For

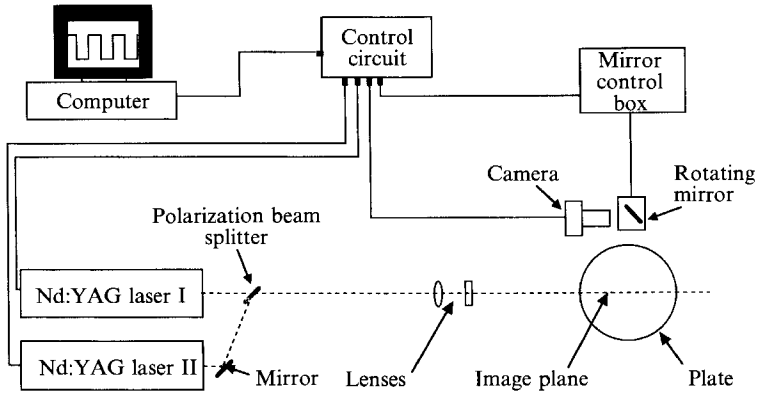

FIGURE 3. PIV data acquisition system.

photographs of smoke, both the jet and the enclosure were seeded. Sufficient numbers of glass particles, however, were confined to the jet core region and the stagnation zone so that little information existed elsewhere in the field of view. Particle mass loading was 2.2% for T7 particles and 3.4% for T2 particles.

Photographs of a single double-pulse event were taken with the same camera and lens mentioned above. To increase overall magnification, an extender ring was placed between the camera body and the lens. T-MAX 400 film was used for gas-phase PIV while Technical Pan film was found to work best for the glass particles.

An artificial image shift was imposed on the flow field to resolve directional ambiguity and to account for the wide range of velocities in the impinging jet. This was accomplished by placing a 45 × 54 mm rotating mirror between the flow and the camera. A scanner, driven by a dedicated controller, oscillated the mirror and measured its angular position. The magnitude of the shift was governed by

$$X_s = 2M\omega_m S_{om}\Delta t \tag{3.1}$$

where S_{om} is the distance from the object plane to the mirror, which was 39.5 cm. For both gas and particle phases, the angular velocity of the mirror ω_m when the lasers fired was 21 rad s^{-1}. The resulting image shift in the film plane was 128 μm corresponding to a horizontal shift velocity of 17 m s^{-1}. The scanner/mirror combination and the camera were protected from particle contamination by a Plexiglas shield. Overall magnification M was 0.49.

The Macintosh computer, linked to a timing circuit, provided the signals necessary to synchronize the components of the PIV system. The camera shutter opening, laser pulsing, and mirror angle were controlled to yield a single double-pulsed event with a predictable image shift for each film exposure. These events were phase locked for forced jet studies.

Analysis of the PIV images was performed by digitizing each film negative with a high-resolution scanner (Nikon Coolscan) linked to a Macintosh computer. Scanner resolution was set at 1350 pixels per inch. Each image file was transferred to a Silicon Graphics Indy workstation and processed with software from Fluid Flow Diagnostics, Inc. The software used a spatial auto-correlation method to calculate the average pixel displacement of image pairs in each interrogation area. The image shift imposed during data collection was subtracted automatically during the interrogation process. Interrogation spot size was set at 64 × 64 pixels, corresponding to a spatial resolution of 2.4 × 2.4 mm at full scale. Interrogation area overlap was set at 50% so that a

54×34 vector field was created for each image file. The resulting displacement vectors were later transformed into velocity vectors by accounting for Δt, M, and scanner resolution. Using a power spectrum, the Kolmogorov scale near the stagnation zone was estimated as approximately 0.1 mm. Therefore, interrogation areas were not small enough to resolve flow microscales.

A small number of vectors in the fluid velocity fields were interpolated using information from surrounding grid points. In most of these files, the percentage of acceptable vectors was nearly 98%. No vectors were interpolated in the particle velocity fields where unacceptable vectors were simply eliminated. The estimated uncertainty in each measurement $\delta U/U_0$ is 2%.

3.3. *Particle number density*

Particle number density maps of the stagnation zone were computed by identifying particles and their corresponding locations in files of the scanned negatives used for PIV. A separate program identified the size and centroid of contiguous clusters of lit pixels. To determine whether the pixel cluster was a single particle or a group of particles, the ratio of the area moments of inertia about the major and minor axes was calculated. Criteria for this ratio and for the number of lit pixels in a cluster were set so that the program could recognize overlapping particle pairs and triplets. Error due to the use of double-pulsed images in the computation of local number density values was negligible.

Number density distributions were plotted on a rectangular grid with the spacing between points corresponding to 53 pixels or 2 mm in real space. The number density at each of four neighbouring grid points was incremented according to particle location. For example, a particle located at the centre of a grid square contributed 0.25 to each corner grid point, whereas a particle located on top of a grid point contributed 1.0 to that grid point. Number densities were normalized by the total number of particles contained in the image file. Typical values for the number of particles per image (accounting for double-pulsing effects) were 2200 for T7 particles and 2000 for T2 particles. To obtain smooth contour plots, a set of at least 16 image files was analysed, summed and normalized for each case examined.

4. Results

A cylindrical coordinate system (r, z) with origin at the stagnation point on the plate is used for the presentation of data. Fluid and particle radial velocities are represented as U_r and V_r, respectively, and axial velocities are represented as U_z and V_z. Coordinate axes and velocities have been non-dimensionalized by the nozzle exit diameter D and the centreline velocity at the nozzle exit U_o respectively. The Reynolds number based on U_o of 10.6 m s^{-1} and D of 3 cm was 21000 for all experiments.

4.1. *Flow visualization and particle number density*

4.1.1. *Unforced flow*

Figure 4 shows instantaneous images of single-phase and multi-phase flow between the nozzle exit and the plate and corresponding number density plots for particle-laden flow in the stagnation zone. Smoke fed into the jet shear layer was used to mark the gas phase. Each contour level on the ensemble-averaged number density plots represents a percentage of the total number of particles counted for each case. Note that the field of view in the plots is not the same as that in the photographs.

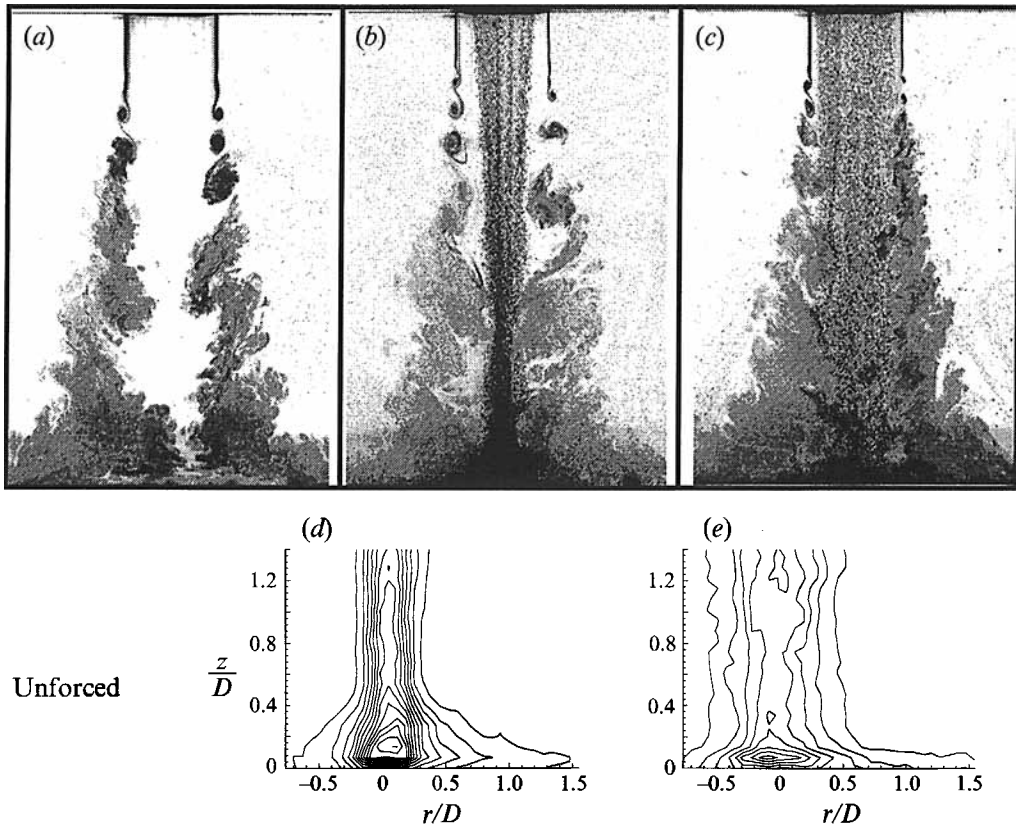

FIGURE 4. Instantaneous images of the flow from the nozzle exit to the plate and particle number density plots in the stagnation zone for the unforced jet. In the number density plots, the lowest contour level is 0.05%, and each successive contour represents an increase of 0.135%. (*a*) Fluid; (*b*) $St_m = 2.4$; (*c*) $St_m = 0.6$; (*d*) $St_m = 2.4$ number density; (*e*) $St_m = 0.6$ number density.

In each photograph, small eddies form initially along the interface between the jet and the surrounding fluid. Downstream, they pair with their neighbours, causing shear layer growth and increases in fluid length scale. As the flow approaches the plate, the vortices grow to the point where the core nearly disappears. The region above $z/D = 1$ will henceforth be referred to as the 'free jet'. In this region, mean velocity and spectral measurements show no discernible effects of a plate downstream.

Downstream of $z/D = 1$, the flow decelerates axially and accelerates radially along the plate causing the vortices to expand. Power spectra obtained with a hot wire located at $(r/D, z/D) = (0.5, 0.02)$ are shown in figure 5. The plots are the result of averaging 50 distinct records of 4096 samples each. The sampling rate was 10.4 kHz. This figure indicates that dominant vortex passage frequencies near the plate range from 120 to 180 Hz, yielding fluid time scales τ_f of 5.6 to 8.3 ms. When the plate is removed, the energy content of the flow shifts to lower frequencies which is consistent with the findings of Gutmark, Wolfshtein & Wygnanski (1978).

Cross-sections of the jet laden with T7 ($St_m = 2.4$) and T2 ($St_m = 0.6$) particles are presented in figures 4(*b*) and 4(*c*) respectively. The photographs show that several factors, each dependent on the particle response time, affect the distribution of particles approaching the stagnation zone. Firstly, particle distribution differs

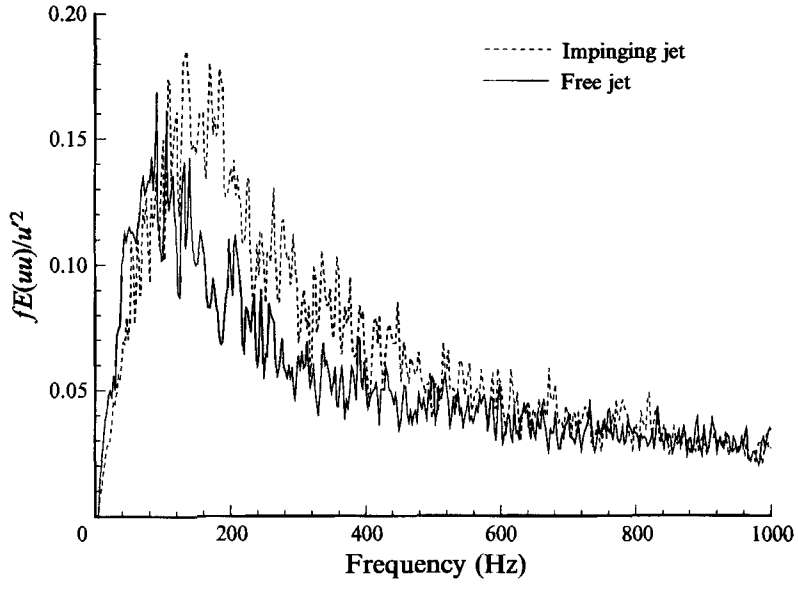

FIGURE 5. Hot-wire power spectra at $(r/D,\ z/D) = (0.5, 0.02)$ with and without the plate installed.

between the two groups at the nozzle exit. T7 particles (higher τ_p) are concentrated near the jet axis, whereas T2 particles (lower τ_p) are dispersed through most of the jet core. This difference in initial distribution occurs because particles with higher inertia acquire and retain larger negative radial velocities through the contraction. Those with lower inertia follow fluid streamlines, which are parallel to the jet axis at the nozzle exit, more closely.

As the flow progresses downstream, the T7 particles become more concentrated near the jet axis, a consequence of the initial conditions and the influence of shear layer vortices. It appears that number density along the jet axis increases steadily all the way to the plate. T2 particles, however, remain evenly dispersed through the jet core as they move downstream. These visual findings are supported by the number density data for each case shown in figure 4(*d*, *e*).

Since the T7 particles are initially relatively far from the shear layer, they do not interact significantly with vortices in the free jet. The particles are 'pinched' toward the jet centreline slightly by larger eddies downstream, but particle dispersion is almost non-existent. Hence, the particles from this group are only slightly disturbed from their downward trajectories as they enter the stagnation zone.

For T2 particles, particle–vortex interactions in the free jet become more important owing to lower τ_p and particle proximity to the shear layer. Perturbations to the particle column appear soon after the particles leave the nozzle. Further downstream, the particle column is alternately pinched toward the jet axis then expanded downstream of vortex cores. Furthermore, particle 'clustering' in the saddle regions between vortices becomes significant close to the plate.

The photographs and number density plots in figure 4 reveal a marked difference between the two groups in stagnation-zone particle distribution. The most striking feature is the large, dense mound formed above the plate for $St_m = 2.4$ in figure 4(*b*). Peak number density (1.1%, in figure 4*d*) occurs directly above the stagnation point, and is almost double the highest value found in the free jet (0.65%). Our hypothesis is that these particles cannot follow the diverging fluid streamlines and, therefore,

must impinge upon and rebound from the plate. Rebound and deceleration cause stagnation zone residence times to lengthen. Above the plate, number density begins to increase at $z/D \approx 0.5$, indicating that rebounding particles are able to reach this height before being forced back toward the plate by the impinging flow. This peak rebound height compares favourably with the height of the particle mound in figure 4(*b*).

The photograph for $St_m = 0.6$ in figure 4(*c*) does not indicate that number density increases in the stagnation zone. The number density plot in figure 4(*e*), however, reveals that concentration levels do increase near the plate but only in a relatively small zone above the stagnation point. Peak number density is 0.7% which, again, is nearly double the highest value found in the free jet for this case (0.4%). Therefore, particle rebound is also an important factor for these more responsive particles, although it is confined to a smaller zone. From these results, it is clear that particle accumulation and distribution in the stagnation zone are heavily dependent on the mean Stokes number St_m.

For a better understanding of particle motion near the plate, particle tracks in the stagnation zone were captured on film and are shown in figure 6. Particle loading for each case was less than 1% of the total mass flux. The photographs show that particle motions near the plate are very complex and that particle rebound is indeed a factor for both particle groups. A variety of particle trajectories are present, representing particles approaching the plate for the first time (primary impinging), particles moving away from the plate (rebounding), and particles re-approaching the plate after reaching the peaks of their rebound trajectories (secondary impinging). It is possible for secondary rebounding particles to exist as well.

For $St_m = 2.4$ in figure 6(*a*), the stagnation zone is saturated with rebounding particles. The ratio of rebounding particles to impinging particles in this zone is about five to one. Particles initially approaching the plate move almost straight downward with little indication of radial motion before impact. Hence, these particles cannot follow fluid streamlines and hit the plate with large vertical velocities. Shortly before impact ($z/D < 0.1$), the average particle axial velocity measured from tracking photographs was 8.5 m s^{-1}. After impact, these particles rebound vertically and travel as far as $z/D = 0.5$ before they are forced back toward the plate by the impinging flow. This height matches well with the height of the particle mound seen in figure 4(*b*) and the location where number density starts to increase in figure 4(*d*). The particles gain some radial momentum along their rebound trajectories, but radial velocities are small until $r/D \approx 0.5$. Because of weak radial acceleration, it appears that multiple particle–wall interactions are possible for this case.

For $St_m = 0.6$ in figure 6(*b*), the stagnation zone is dominated by primary *impinging* particles. Rebounding particles are significant only below $z/D \approx 0.1$, which is where number densities are highest (see figure 4*e*). As in the previous case, particle trajectories near the jet axis are virtually straight down before impact. However, these more responsive particles decelerate more quickly before and after impact and remain relatively close to the plate where fluid radial velocities (and thus radial drag) are highest. Average impact velocity for these particles was 6.5 m s^{-1}. Notice that particles away from the jet axis follow trajectories which are noticeably curved in the positive radial direction. Consequently, many of these particles strike the plate obliquely and rebound away from the stagnation zone.

The above results for the unforced jet show that the regions of highest particle concentration correspond to regions where particle rebound is predominant. The photographs also show a strong correlation between rebound and mean Stokes

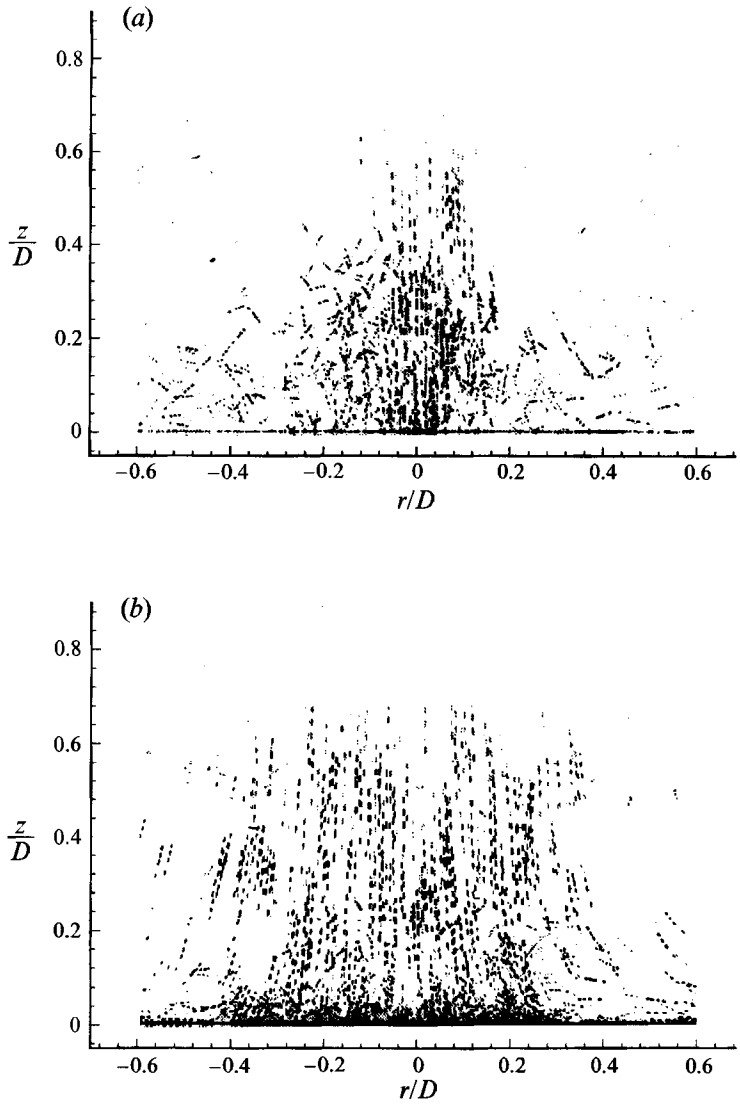

FIGURE 6. Particle trajectories in the stagnation zone. (*a*) $St_m = 2.4$; (*b*) $St_m = 0.6$.

number St_m. Any effect of vortices on particle motion and distribution near the plate is unclear, however.

4.1.2. *Forced flow*

In order to clarify particle–vortex interactions near the plate, the jet was forced acoustically at a frequency f of 180 Hz, corresponding to a Strouhal number Sr_D of 0.51 where Sr_D is defined as fD/U_0. The frequency and forcing amplitude were chosen so that evenly spaced, repeatable vortex rings persisted down to the impingement surface. The forcing amplitude produced an r.m.s. velocity u'/U_o of 0.1 at the nozzle exit. Laser illumination was phase locked with the forcing cycle at phase angles Φ of 0°, 90°, 180°, and 270°.

Cross-sectional images and corresponding particle number density plots in the stagnation zone at each of the four phases are shown in figures 7–10. Single-phase

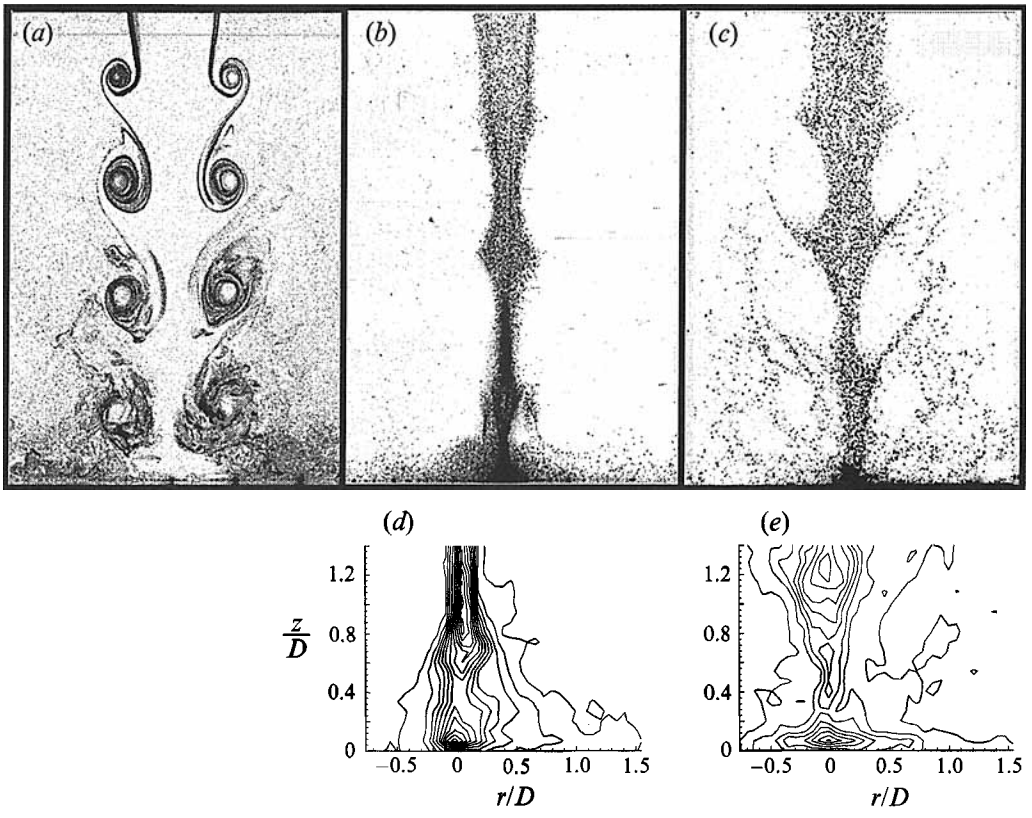

FIGURE 7. Instantaneous images of the flow from the nozzle exit to the plate and particle number density plots in the stagnation zone for the forced jet ($Sr_D = 0.51$, $\Phi = 0°$). In the number density plots, the lowest contour level is 0.05%, and each successive contour represents an increase of 0.135%. (*a*) Fluid; (*b*) $St' = 1.25$; (*c*) $St' = 0.3$; (*d*) $St' = 1.25$ number density; (*e*) $St' = 0.3$ number density.

and particle-laden flow are shown separately so that particle concentration near the plate can be seen more clearly. Unlike in the natural jet, large-scale vortex rings form near the nozzle exit. Vortex pairing does not occur, and the length scale between successive vortex cores remains constant through the free jet. The propagation velocity of each ring is 6.1 m s^{-1}, and the vortex time scale τ_f is 5.6 ms. Near the plate, vortex ring locations and resulting flow patterns are strongly phase dependent.

Images and number density plots of T7 particles ($St' = Sr_D\, St_m = 1.25$) are shown in (*b*) and (*d*) respectively in figures 7–10. From the photographs, we see that in the free jet, forcing causes the particles inside each vortex ring to become highly concentrated near the jet axis, more so than in the unforced case. Between successive vortex rings, but nearer the downstream ring, the particles form diamond-shaped clusters. As the clusters move downstream, they approach the centres of the downstream vortices. Subsequently, these vortices retard particle dispersion by forcing particles toward the jet axis (see figures 7*b* and 10*b*). The number density plots in figures 7(*d*) and 10(*d*) confirm this, showing that particle concentration increases near the jet axis as the flow moves downstream. At $\Phi = 90°$, concentration levels near the axis reach a maximum of 1.5% at $z/D \approx 0.5$, and the 'clusters' lose their coherence as they approach the plate (see figure 8*b*, *d*). Cluster impingement occurs at $\Phi = 180°$.

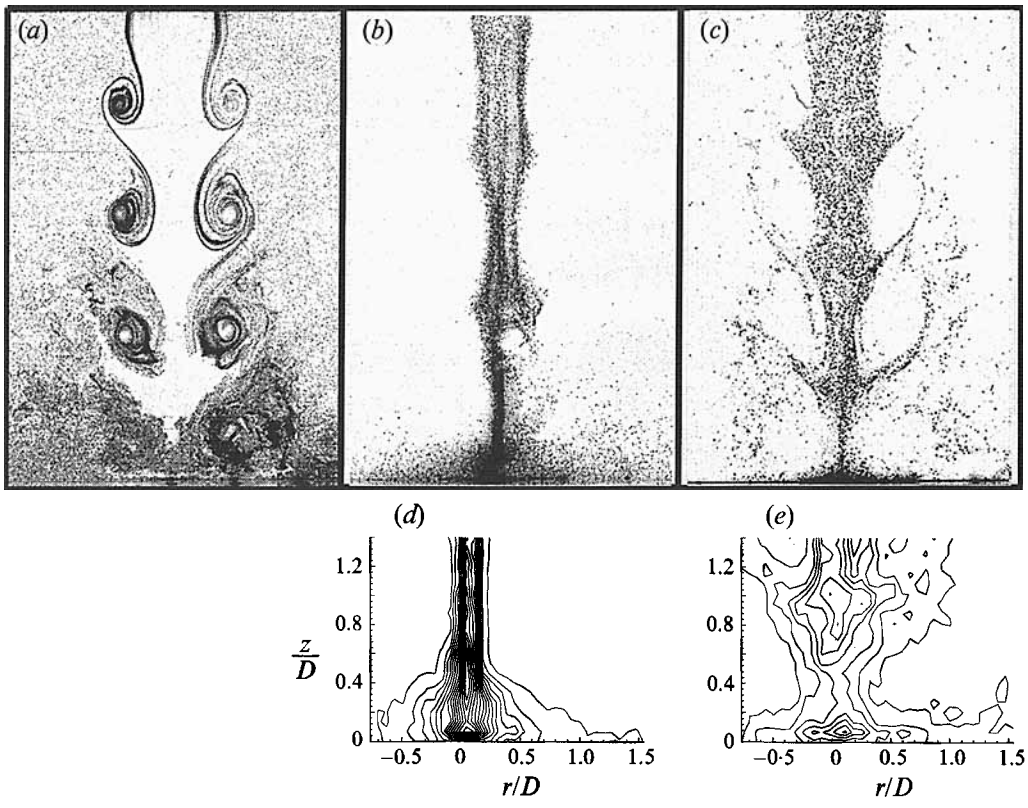

FIGURE 8. Instantaneous images of the flow from the nozzle exit to the plate and particle number density plots in the stagnation zone for the forced jet ($Sr_D = 0.51$, $\Phi = 90°$). In the number density plots, the lowest contour level is 0.05%, and each successive contour represents an increase of 0.135%. (*a*) Fluid; (*b*) $St' = 1.25$; (*c*) $St' = 0.3$; (*d*) $St' = 1.25$ number density; (*e*) $St' = 0.3$ number density.

Near the plate, particle concentration and distribution have some phase dependence. Peak number density values vary from 1.3% at $\Phi = 90°$ and 180° to 1.0% at $\Phi = 270°$. Notice that particles are most densely packed about the stagnation points at $\Phi = 90°$ and $\Phi = 180°$ when the vortices and particle clusters impinge upon the plate. The height of the particle mound in the stagnation zone does not change noticeably with phase, except at $\Phi = 180°$ when it appears slightly shorter than average.

Photographs and number density plots of T2 particles ($St' = Sr_D St_m = 0.3$) are shown in (*c*) and (*e*) respectively in figures 7-10. Forcing produces more dramatic effects on the motion and distribution of these more responsive particles. The features in the free jet are similar to those seen in the previous case, but particle dispersion is now significant. Many particles are flung across the shear layer by the vortex-induced radial velocity field. The particles that remain in the shear layer associate with a single vortex ring as they move downstream. The clusters that form between successive vortex rings are closer to the upstream ring. Consequently, the clusters are not pulled apart by the downstream vortex as in the previous case and are well defined as they approach the plate (see figure 9*c*).

The clusters impact the plate at $\Phi = 270°$ well ahead of the impinging vortex ring (figure 10*c*) and subsequently disintegrate by $\Phi = 0°$ (figure 7*c*). At the latter

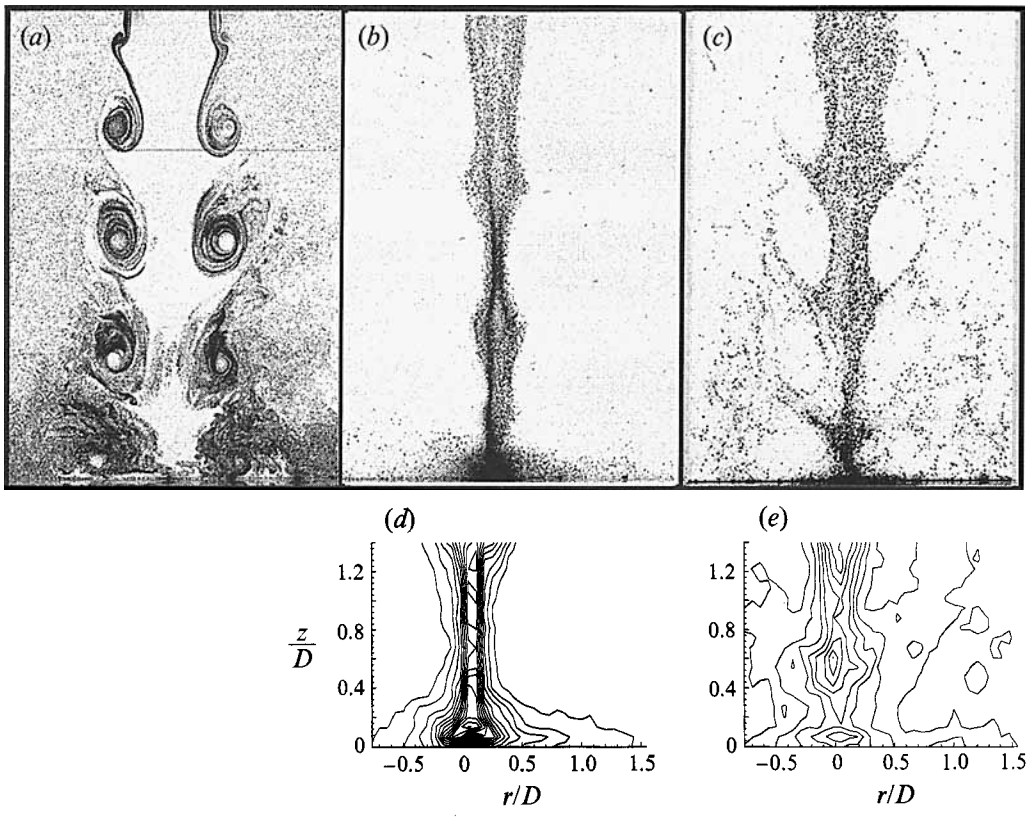

FIGURE 9. Instantaneous images of the flow from the nozzle exit to the plate and particle number density plots in the stagnation zone for the forced jet ($Sr_D = 0.51$, $\Phi = 180°$). In the number density plots, the lowest contour level is 0.05%, and each successive contour represents an increase of 0.135%. (*a*) Fluid; (*b*) $St' = 1.25$; (*c*) $St' = 0.3$; (*d*) $St' = 1.25$ number density; (*e*) $St' = 0.3$ number density.

phase, number density reaches its peak (0.75%) above the stagnation point as shown in figure 7(*e*). This value is comparable to the highest concentration level in the unforced jet for this particle group. During vortex impingement ($\Phi = 90°$ and 180°), particle concentration above the stagnation point decreases significantly. By $\Phi = 180°$, the peak number density value near the plate is 50% less than the peak value at $\Phi = 0°$. The particles remaining near the stagnation point at $\Phi = 180°$, which were once *downstream* of the impinging ring, are now *upstream* of the vortex.

The vortices in the free jet produce time-dependent variations in particle concentration in the stagnation zone. The variations are more significant for lower St'. Particles dispersed into the shear layer in the free jet can remain downstream of the vortex after impingement. This occurs for $St' = 0.3$ only. Those that hit the plate near the stagnation point (both $St' = 0.3$ and 1.25) fall behind the impinging vortex ring. Hence, these particles either trail the ring as they leave the stagnation zone or become associated with the next vortex to approach the plate (i.e. they skip a cycle). The latter behaviour is predominant for $St' = 1.25$ due to the relatively long particle residence times in the stagnation zone.

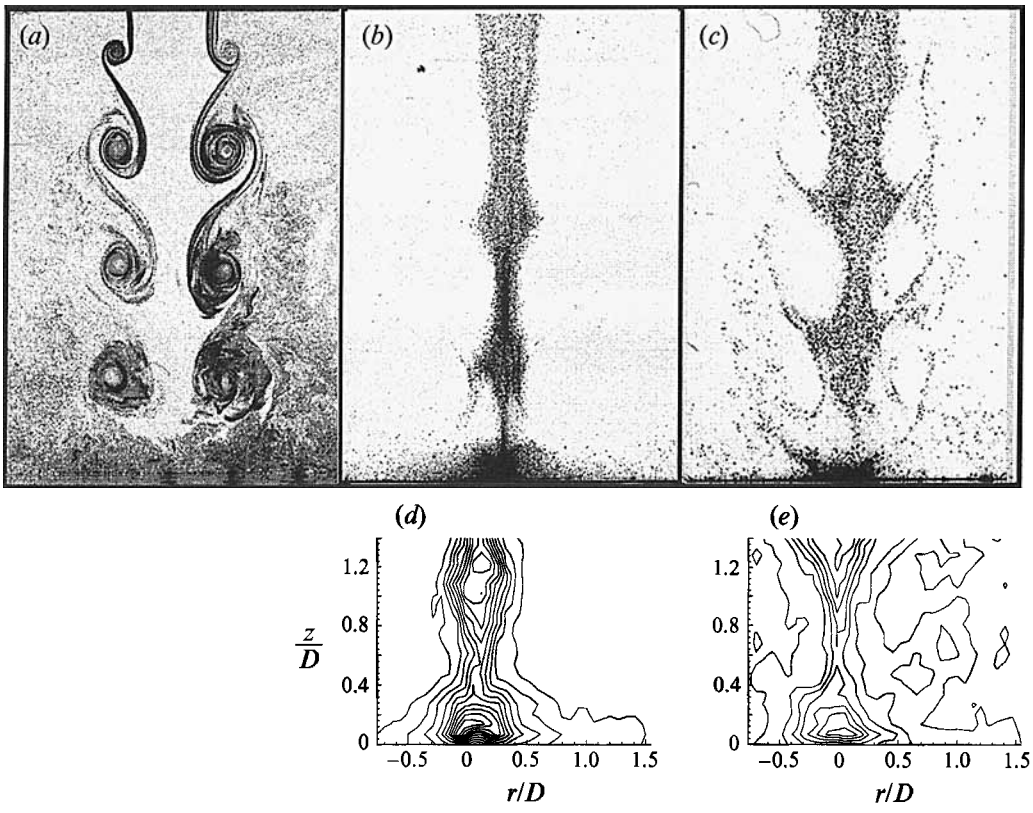

FIGURE 10. Instantaneous images of the flow from the nozzle exit to the plate and particle number density plots in the stagnation zone for the forced jet ($Sr_D = 0.51$, $\Phi = 270°$). In the number density plots, the lowest contour level is 0.05%, and each successive contour represents an increase of 0.135%. (*a*) Fluid; (*b*) $St' = 1.25$; (*c*) $St' = 0.3$; (*d*) $St' = 1.25$ number density; (*e*) $St' = 0.3$ number density.

4.2. *Gas-phase velocity fields*

4.2.1. *Unforced flow*

Instantaneous and ensemble-averaged fluid velocity fields are shown in figure 11. The field of view is the same as that used in the particle number density studies. Downward velocities are defined to be negative. The ensemble-averaged field was computed from 16 instantaneous files. The instantaneous fields illustrate the time-dependent nature of the flow and reveal the presence of shear layer vortices. The vortices, which range in length scale from about $0.5D$ to $1D$ ($3 \leqslant \tau_f \leqslant 6$ ms), produce easily distinguishable disturbances on the flow field even in the absolute reference frame. The disturbances in the shear layer are seen most clearly where spatial velocity variations are large. The eddies are not necessarily ring-like, and asymmetric velocity fields are often observed. These fields are similar in nature to those found by Landreth & Adrian (1990).

In the core of the free jet, instantaneous fluid velocities upstream of $z/D = 1$ are primarily in the axial direction and in the range $-0.9 \leqslant U_z/U_o \leqslant -1.15$. The fluid slows gradually to approximately $-0.6U_o$ at $z/D = 0.25$, then decelerates quickly as it approaches the plate. Subsequently, the fluid accelerates rapidly along the plate, reaching dimensionless radial velocities (U_r/U_o) of 0.6 by $r/D = 0.5$ and 0.75 by

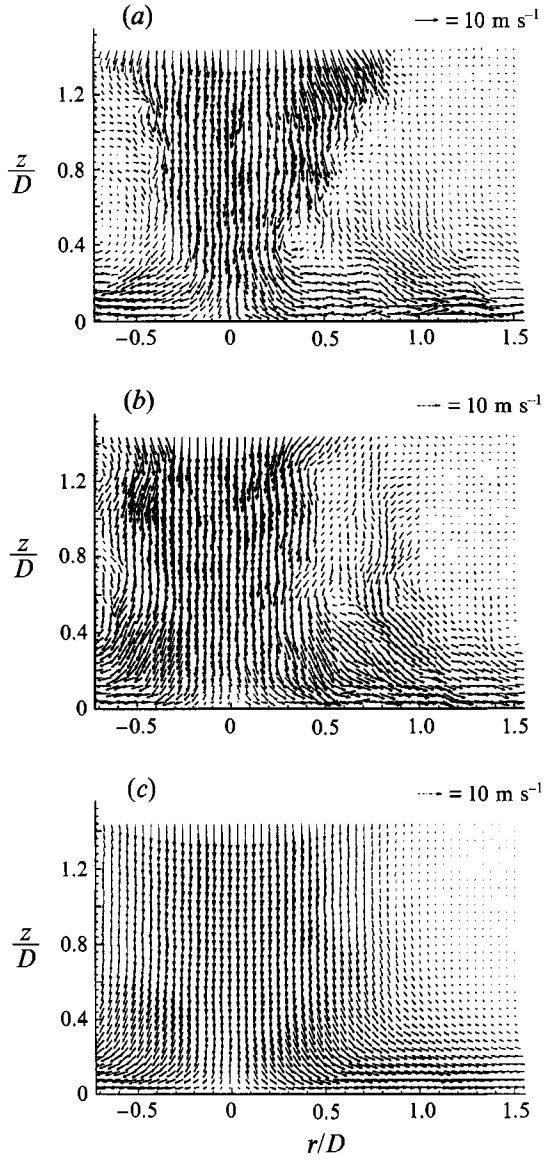

FIGURE 11. Absolute velocity fields of the gas phase in the unforced jet: (*a*) and (*b*) instantaneous fields; (*c*) ensemble-averaged field.

$r/D = 1$. Radial velocities are largest in the row of vectors closest to the plate. Notice that the radial flow along the plate is also affected by the presence of large-scale eddies.

Comparison of the two instantaneous vector fields reveals significant velocity variations near the plate. For instance, to the right of the jet centreline near $r = 0.4D$, most velocity vectors are horizontal in figure 11(*a*), while they are nearly vertical in figure 11(*b*). Specifically, at $(z/D, r/D) = (0.2, 0.4)$ in figure 11(*a*), the velocity components are $(U_r, U_z) = (3.9, -0.6)$ m s^{-1}. At the same location in figure 11(*b*), the velocity components are (3.1, −6.5). These results illustrate the large impact of vortices on the flow and thus the possibility that they can affect particle motions near

the plate. Note, however, that the flow field for $r/D \leqslant 0.3$ is virtually the same in both instances.

The ensemble-averaged flow field in figure 11(*c*) represents to a reasonable degree the time-averaged behaviour of the jet. Evidence of shear layer disturbances disappears. The figure shows a very uniform flow that decelerates smoothly as it nears the plate. Radial velocities first become important at the edge of the jet at $z/D \approx 0.7$. As the flow moves further downstream, increases in the radial component of velocity migrate toward the jet centreline, but radial velocity dominates the flow only below $z/D \approx 0.1$. Very close to the plate, the fluid accelerates rapidly from the stagnation point out to $r/D \approx 1.0$. Beyond this location, the fluid in the wall jet decelerates.

4.2.2. *Forced flow*

Four phase-locked, ensemble-averaged fluid velocity fields of the forced jet are shown in figure 12. Ten instantaneous files were used to compute each averaged field. At first glance, these average fields appear quite different from the average velocity field of the unforced jet. Clearly, the vortex rings induce large disturbances in both axial and radial directions in the shear layer of the free jet. In the stagnation zone, strong radial velocities are induced downstream of the rings as they approach the plate (see figure 12*a*, *b*). Notice that vortex effects are small near the jet axis, however. Near the stagnation point, the flow fields of the forced and unforced jets look similar. Hence, the plate damps out vortex-induced variations there. As the rings expand radially into the wall jet ($\Phi = 180°$ and $\Phi = 270°$), maximum radial velocities between the plate and vortex cores are nearly twice the propagation velocity of the rings.

The ensemble-averaged, *relative* velocity fields in figure 13 show more clearly the differences between the forced and unforced jets at each phase of the forcing cycle. The plots are the result of subtracting the unforced ensemble-averaged velocity field from the forced ensemble-averaged velocity fields. While the differences between the forced and unforced jets are fairly significant in the free jet and the wall jet, they are small in the stagnation zone.

Near the ring cores, vortex-induced velocities are large. However, in the region bounded by $r/D \approx 0.5$ and $z/D \approx 0.5$, which is where particles from both groups are most highly concentrated, the effects of the vortices are nearly insignificant. We suspected that the vortices would induce strong radial velocities through a larger percentage of the stagnation zone and thus would be effective in 'sweeping' particles into the wall jet. At $\Phi = 0°$ and 90°, the vortices do increase fluid radial velocities near the plate, but only for $r/D \geqslant 0.4$. Thus, at these two phases, the vortices could increase particle evacuation rates from the stagnation zone, but only those particles in the vicinity of the ring would be affected. For $\Phi = 90°$, radial velocities above $z/D \approx 0.2$ are actually smaller than in the unforced flow and thus radial drag may be reduced in this region at this phase. At $\Phi = 180°$ and 270°, the vortices have virtually no effect on either radial or axial velocities in the stagnation zone.

From the fluid velocity fields of the unforced and forced jets in the stagnation zone, it is clear that the effects of vortices in the flow are limited to the shear layer region. Hence, St' is an important parameter only for those particles in the vicinity of the rings. In the region above the stagnation point where particles from both groups are highly concentrated, the flow fields of the unforced and forced jets are quite similar. For particles that reside here, the mean flow parameters (and therefore St_m) prevail in determining particle motions.

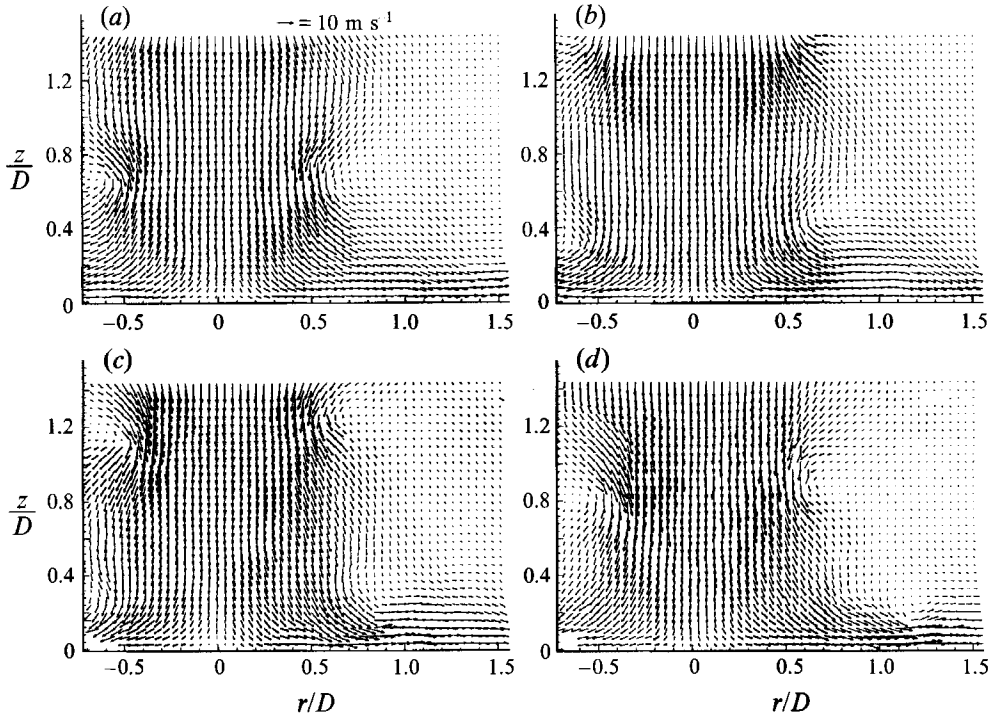

FIGURE 12. Ensemble-averaged velocity fields of the gas phase in the forced jet ($Sr_D = 0.51$). (*a*) $\Phi = 0°$; (*b*) $\Phi = 90°$; (*c*) $\Phi = 180°$; (*d*) $\Phi = 270°$.

4.3. *Particle-phase velocity fields*

4.3.1. *Unforced flow*

Figures 14 and 15 show instantaneous and ensemble-averaged velocity fields for $St_m = 2.4$ and 0.6 respectively. Note that vectors appear only where there is sufficient information for the autocorrelation calculation. The ensemble-averaged vector fields were calculated from at least 16 instantaneous files, and any missing vectors were ignored. Thus, in areas of low particle number density or in areas with 'noisy' correlations, fewer vectors were averaged. Relative velocity fields ($\langle U \rangle - \langle V \rangle$) were computed by subtracting each averaged particle vector from the corresponding averaged fluid vector. The resulting vector fields reveal the direction of the average drag force on the particles in each interrogation region.

In (*a*) and (*b*) of figures 14 and 15, the distribution of vectors in the instantaneous fields changes with time, due presumably to the effects of large shear layer vortices upstream of the stagnation zone. Particle velocities are primarily in the axial direction throughout the free jet for both cases. For $St_m = 0.6$, however, particles near the shear layer generally possess detectable radial velocities as they approach the plate. Typical dimensionless axial speeds between $z/D = 1.4$ and $z/D = 1.0$ are in the range of 0.95–1.05 for $St_m = 2.4$ and 0.95–1.15 for $St_m = 0.6$. As the particles continue downstream, they decelerate more slowly than the fluid, losing only a fraction of their momentum before they interact with the plate. Recall that dimensionless average speeds just before impact are 0.85 for $St_m = 2.4$ and 0.65 for $St_m = 0.6$.

Owing to rebound, the particle flow field near the plate is extremely complicated (see figure 6). Therefore, it is important to address the actual meaning of the PIV

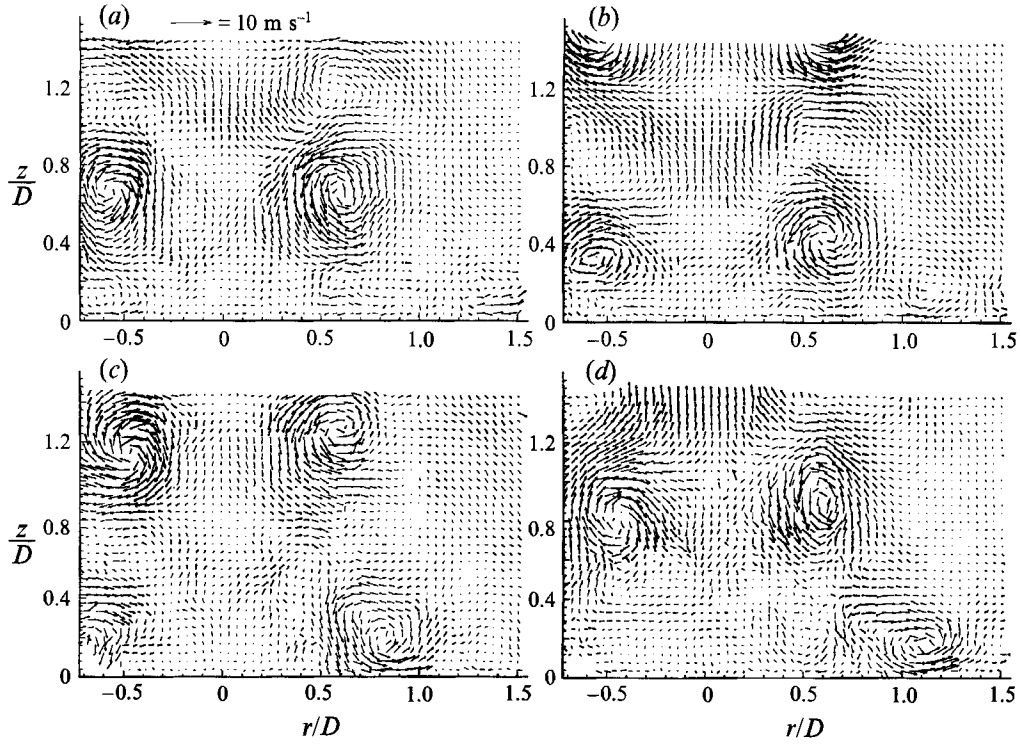

FIGURE 13. Ensemble-averaged relative velocity fields ($\boldsymbol{U}_{\text{forced}} - \boldsymbol{U}_{\text{unforced}}$) of the fluid in the forced jet ($Sr_D = 0.51$). (*a*) $\Phi = 0°$; (*b*) $\Phi = 90°$; (*c*) $\Phi = 180°$; (*d*) $\Phi = 270°$.

results in the stagnation zone. In each interrogation region, the strongest peak in the autocorrelation function corresponds to the most prevalent particle displacement. This peak is used to compute a velocity vector. In a region where impinging particles prevail but are not exclusive (i.e. rebounding particles are present) PIV 'sees' only the impinging particles. Information about the rebounding particles is essentially ignored. Likewise, in regions where rebounding particles are predominant, the PIV vector ignores information about impinging particles. If the autocorrelation contains no significant peak, no vector is calculated. As a result, the velocity vectors in the stagnation zone do not represent true spatial averages. Rather, they are biased toward the dominant behaviour in the interrogation zone at that instant. Thus, the vectors shown represent the prevailing velocities in each interrogation zone. Averaged vectors then represent the average of the 'dominant' behaviour in a given zone (for further explanation, see Anderson 1995).

Comparison of the instantaneous vector fields in the stagnation zone reveals that rebounding particles occupy a larger percentage of this region for larger St_m, supporting both flow visualization and particle number density results. For $St_m = 2.4$, vectors corresponding to rebounding particles predominate and are found up to $z/D \approx 0.5$ in figure 14(*a*, *b*). Impinging particle vectors are found along the jet axis only. The magnitude and direction of rebound vectors at a given flow location depend on particle histories. For instance, to the right of $r/D = 0.2$ in figure 14(*a*), the vectors indicate strong upward velocities. Conversely, particles reaching the peaks of their rebound trajectories and returning to the plate prevail in the same region in figure 14(*b*). In both instances, particle velocities are predominantly horizontal beyond $r/D \approx 0.5$. As

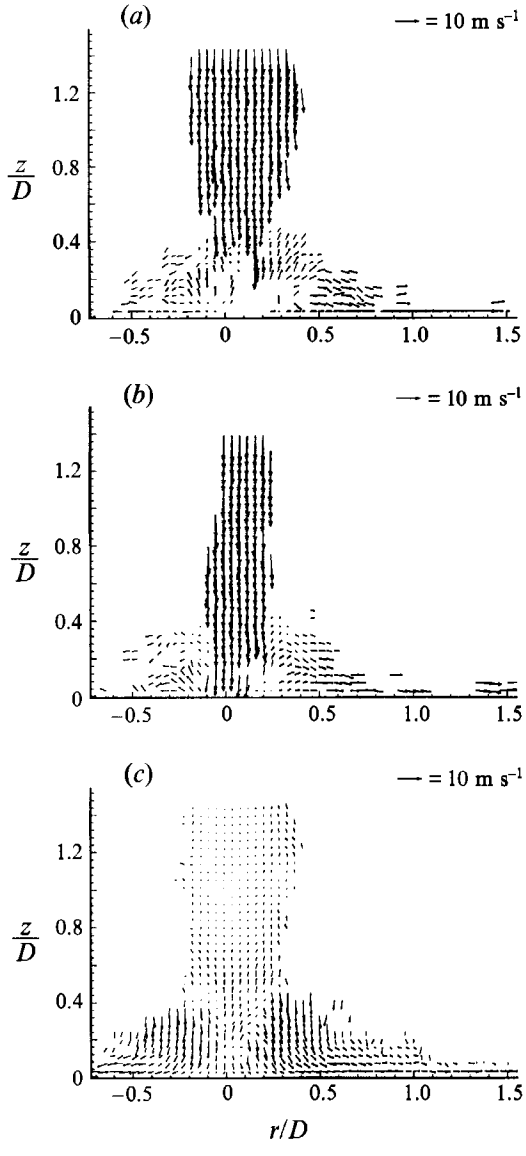

FIGURE 14. Particle velocity fields for $St_m = 2.4$. (*a*) and (*b*) instantaneous absolute; (*c*) ensemble-averaged relative ($\langle U \rangle - \langle V \rangle$).

r/D increases, sufficient numbers of particles for the autocorrelations (hence vectors) are found only near the surface of the plate.

The instantaneous velocity fields in figure 15(*a*, *b*) for $St_m = 0.6$ show that primary impinging particles prevail almost to the plate. Velocities corresponding to rebounding particles are significant in only a small percentage of the interrogation regions near the plate. These particles, which respond to fluctuations in the fluid four times as fast as the other group, lose their axial momentum quickly after impact and remain close to the plate where fluid radial velocities (thus drag) are highest. Particle radial velocities along the plate at $r/D > 0.5$ are noticeably larger for this case than for $St_m = 2.4$.

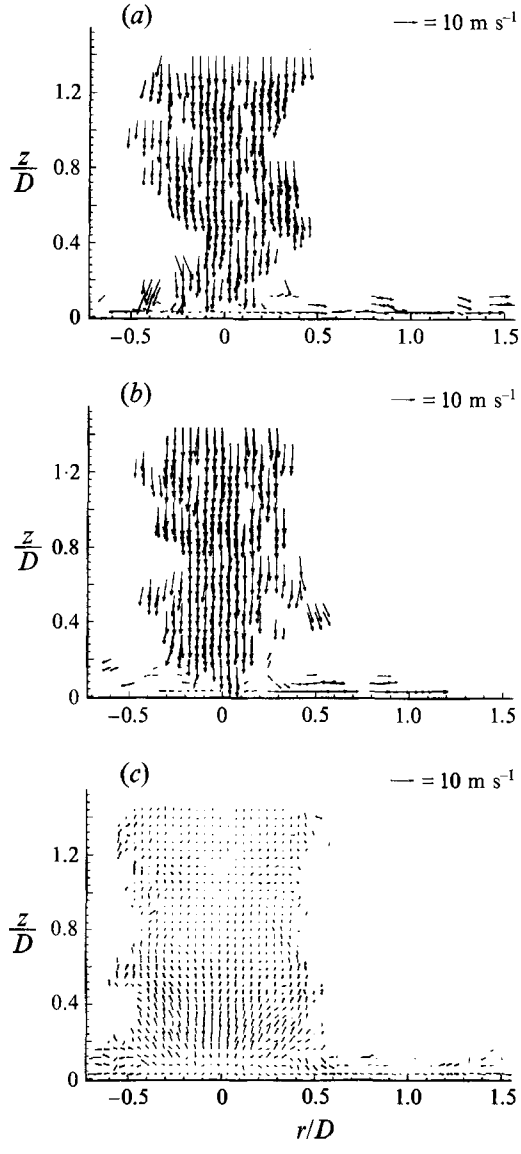

FIGURE 15. Particle velocity fields for $St_m = 0.6$: (*a*) and (*b*) instantaneous absolute; (*c*) ensemble-averaged relative ($\langle U \rangle - \langle V \rangle$).

For both cases, particle velocity vectors near the stagnation point are generally very small. This indicates that particles moving very slowly due to single or multiple interactions with the plate are nearly always prevalent in this region.

For each particle group, ensemble-averaged relative velocity fields ($\langle U \rangle - \langle V \rangle$) are shown in figures 14(*c*) and 15(*c*). In general, upward slip vectors indicate where impinging particles are predominant, and downward slip vectors indicate where rebounding particles are predominant. In the free jet, particles and fluid are travelling at roughly the same speed. Particles near the shear layer tend to move slightly faster than the fluid. As the flow enters the stagnation zone, the fluid and particles decelerate at different rates, and the particles from each group lead the fluid in the

axial direction. Slip velocities increase both axially and radially as the flow moves downstream through the deceleration zone.

Downstream of $z/D = 0.5$, the relative velocity fields differ significantly between the particle groups. For $St_m = 2.4$ in figure 14(*c*), primary impinging particles are predominant only near the jet centreline down to $z/D \approx 0.2$. Elsewhere, particles moving much more slowly than the fluid dominate owing to interactions with the boundary. These particles experience strong axial drag, especially those above $z/D \approx 0.2$. As these heavier particles rebound from the plate they enter regions where radial drag is not significant. Therefore, these particles do not feel strong radial acceleration until they are forced back nearer the plate where fluid radial velocities are higher. Hence, the prevailing fluid velocity field is not effective in accelerating these particles out of the stagnation zone quickly, resulting in the observed high number densities there.

Figure 15(*c*) shows that a majority of the lighter particles ($St_m = 0.6$) above $z/D \approx 0.1$ lead the fluid in the axial direction. Those in close proximity to the shear layer experience considerable drag in the radial direction as they approach the plate, starting at $z/D \approx 0.5$. Consequently, many of these particles acquire radial velocity *before* they hit the plate, unlike the case of $St_m = 2.4$ where the particles are situated too close to the jet axis to feel significant radial drag. Negative axial slip is important only near $r/D = 0.5$ where rebounding particles moving radially outward are pulled closer to the plate by the diverging, impinging fluid. In general, radial slip velocities along the plate are smaller for $St_m = 0.6$, implying that these particles have larger radial velocities and exit the stagnation zone more quickly. Consequently, particle concentration levels near the plate are lower for this case.

4.3.2. *Forced flow*

Ensemble-averaged relative particle velocity fields were computed for $St' = 1.25$ and 0.3 at each phase of the forced jet and are shown in figures 16 and 17 respectively. The highest contour levels of the fluid vorticity field are plotted at each phase to indicate the relative positions of the vortices. These figures show the periodicity of the drag forces on the particles at a given spatial location.

For $St' = 1.25$ in figure 16, particles near the upstream side of vortices in the free jet feel downward and inward drag, while those in the saddle regions between successive vortices feel upward drag. Interestingly, when the absolute velocity fields of particles in the forced and unforced jets are compared, the differences are small in the free jet. This is true at each phase of the forcing cycle. Hence, the periodic concentration of T7 particles near the jet axis due to vortices must result from long time effects.

In the stagnation zone, the distribution of slip velocities (i.e. drag) is noticeably phase dependent. This phase dependence is due to the particle histories that are most prevalent at each phase. Common to all phases are large, negative axial slip velocities away from the jet axis indicating that rebounding particles are always prevalent there. Fast moving, impinging particles generally dominate near the jet axis down to $z/D \approx 0.2$. At $\Phi = 0°$ and 270° in figure 16(*a*) and 16(*d*) respectively, slow moving, rebounding particles are prevalent over a large percentage of the stagnation zone as indicated by strong axial drag toward the plate. Recall that these two phases correspond to times when the influx of impinging particles is reduced and particles are more widely distributed through the region (see figures 7*d* and 10*d*). Therefore, rebounding particles are more dominant during these two phases. Radial drag is significant only for those particles beneath the vortex in the wall jet. As vortices and particle clusters approach the plate ($\Phi = 90°$ in figures 8*a*, *d*, and 16*b*), particles

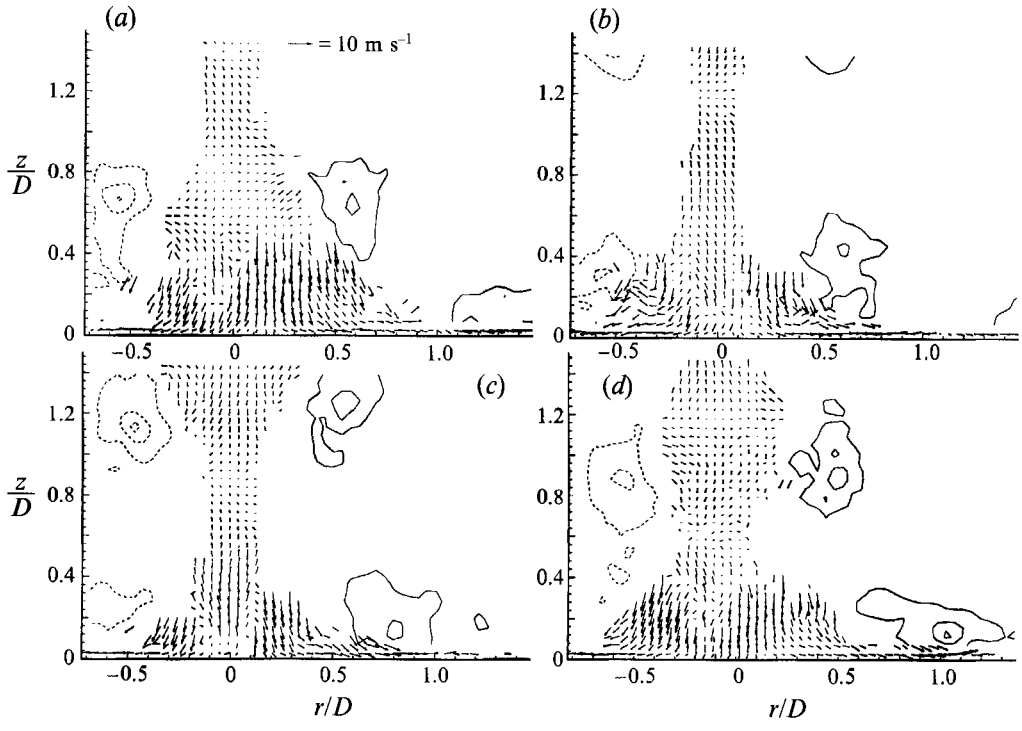

FIGURE 16. Ensemble-averaged relative particle velocity fields ($\langle U\rangle - \langle V\rangle$) for the forced jet; $Sr_D = 0.51$ and $St' = 1.25$. The vorticity contour lines indicate the positions of vortices in the fluid. (*a*) $\Phi = 0°$; (*b*) $\Phi = 90°$; (*c*) $\Phi = 180°$; (*d*) $\Phi = 270°$.

with both impinging and rebounding trajectories seem to be important. Radial slip velocities in the region neighbouring $r/D = 0.5$ are larger than at $\Phi = 0°$ owing to the impinging vortex. At $\Phi = 180°$ in figure 16(*c*), when a dense cluster of particles hits or is about to hit the plate, primary impinging particles are more dominant near the jet axis than in the other phases. Away from the centreline, large negative slip velocities (thus strong rebound) are apparent. Note, however, that rebounding particles occupy a smaller percentage of the stagnation zone than in the other three phases.

For $St' = 0.3$ in figure 17, specific patterns in the relative velocity fields are less obvious. In the free jet, particles near the axis generally move at the same rate as the fluid. Near the shear layer, particles downstream of a vortex are accelerated radially outward by the fluid as shown in figures 17(*a*) and 17(*b*), but those upstream of a vortex are pushed back toward the jet centreline (top of figure 17*d*). In the stagnation zone, impinging particles which lead the fluid generally dominate the field above $z/D \approx 0.2$. Thus, rebounding particles are rarely significant above this height. Impinging particles are especially prominent at $\Phi = 270°$ in figure 17(*d*) when the particle clusters are about to hit the plate (refer to figure 10*c*). Radial drag is also significant over most of the stagnation zone at this phase. Rebounding particles, thus negative axial slip velocities, are strongest at $\Phi = 0°$. By $\Phi = 180°$, when number density reaches a minimum for this case, the region close to the plate is nearly devoid of information. Except for $\Phi = 270°$, radial slip is significant only in the first row of vectors at each phase. Beneath the vortex cores in the wall jet where fluid velocities are exceptionally high, radial slip velocities are largest.

The particle velocity fields for both the unforced and forced jet reinforce the

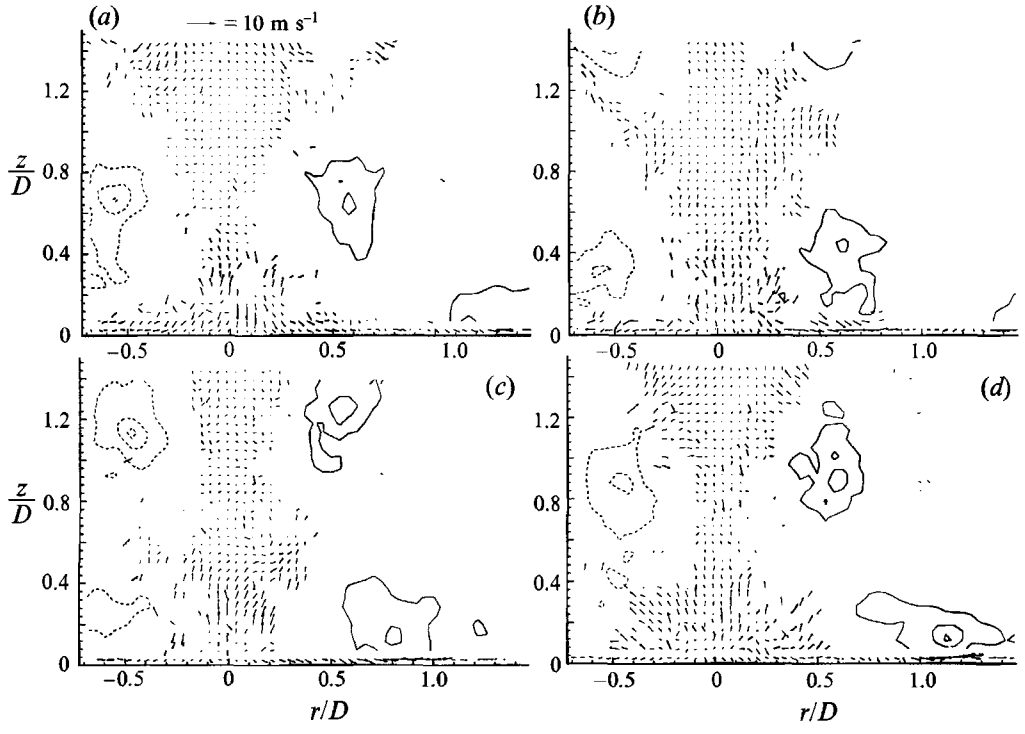

FIGURE 17. Ensemble-averaged relative particle velocity fields ($\langle U\rangle - \langle V\rangle$) for the forced jet; $Sr_D = 0.51$ and $St' = 0.3$. The vorticity contour lines indicate the positions of vortices in the fluid. (*a*) $\Phi = 0°$; (*b*) $\Phi = 90°$; (*c*) $\Phi = 180°$; (*d*) $\Phi = 270°$.

hypothesis that the mean flow (i.e. St_m) is the major factor affecting the motion of particles in the stagnation zone. The influence of vortices (i.e. St') is limited to regions local to the shear layer. Hence, only particles that are dragged into the shear layer prior to impact and particles that have migrated to large enough r/D along the plate feel the effects of the vortex-induced velocity field.

4.4. *Modelled flow*

To compare with the experimental results, we computed particle velocities along the jet centreline from a simplified equation of motion including only drag and gravitational forces. Since the density of the particles is much larger than the density of the fluid, contributions from the terms concerning added mass and fluid pressure are small and were neglected. Estimates of the Basset history force in the stagnation zone were also found to be negligibly small. Therefore, the governing equation used was

$$\frac{\mathrm{d}V}{\mathrm{d}t} = \frac{\phi}{\tau_p}(U - V) + g \tag{4.1}$$

where $\phi = (1+0.15\ Re_p^{0.687})$ is an empirical non- Stokesian drag factor (Clift, Grace & Weber 1978). The model traced the axial motion of a single particle from the nozzle entrance to the plate under the influence of the unforced jet along the centreline. It also computed particle rebound height and particle velocity prior to a second collision with the plate. The model assumed zero slip velocity at the nozzle entrance and perfectly elastic collisions with the plate.

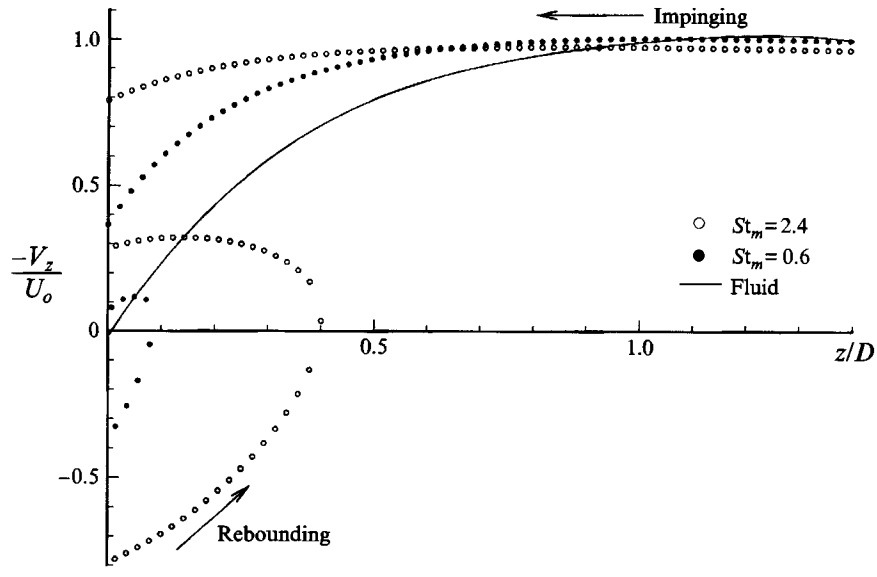

FIGURE 18. Modelled particle motion along the jet centreline.

The results, plotted in figure 18, show the predicted velocity of an average particle from each group. A 30 μm T7 particle ($St_m = 2.4$) slows very little as it approaches the plate whereas a 40 μm T2 particle ($St_m = 0.6$) decelerates to less than half of its free jet velocity. After impact, slip velocities can be very high, resulting in significant values of particle Reynolds number (Re_p). Maximum Re_p for $St_m = 2.4$ and $St_m = 0.6$ are 20 and 11 respectively. Owing to large upward momentum, a T7 particle travels to about $z/D = 0.4$ before stalling, whereas a T2 particle rebounds to only $z/D = 0.1$. These values are in good agreement with the observed heights of particle mounds, the locations where number density starts to increase in the stagnation zone (figure 4), and the height to which the particles rebound from the plate (figure 6).

Figure 19 compares measured and computed radial particle velocities in the plane $z/D = 0.04$, which is the lower bound of the measured field. The measured velocities were extracted from the ensemble-averaged particle velocity fields. For the computed velocities, the radial velocity distribution of the fluid was input into the model, and the motion of a representative particle from each group was followed. Initial particle velocities at $r/D = 0$ were non-zero ($< 0.05U_o$) to maintain model stability. Fluid velocity is also plotted in the figure to show relative slip velocities for each group.

As expected, the measured data show that particles invariably lag the fluid in the radial direction. For $St_m = 2.4$, particles are the most sluggish and lag the fluid by as much as $0.35U_o$ in the region $0.3 \leqslant r/D \leqslant 1.0$. In the same region, slip velocities for $St_m = 0.6$ are considerably less. The particles appear to accelerate steadily out to $r/D \approx 1$. It is surprising that the measured data compare quite favourably with the computed velocities out to $r/D \approx 1$. We expected that the measured radial velocities would be noticeably less than the predicted values because of particles rebounding through the zone of highest radial velocity. However, these results suggest that a significant number of particles from each group lose vertical momentum near the jet centreline, through either single or multiple rebounds, then accelerate radially close to the plate.

Beyond $r/D = 1$, the data points become widely scattered, but almost all of

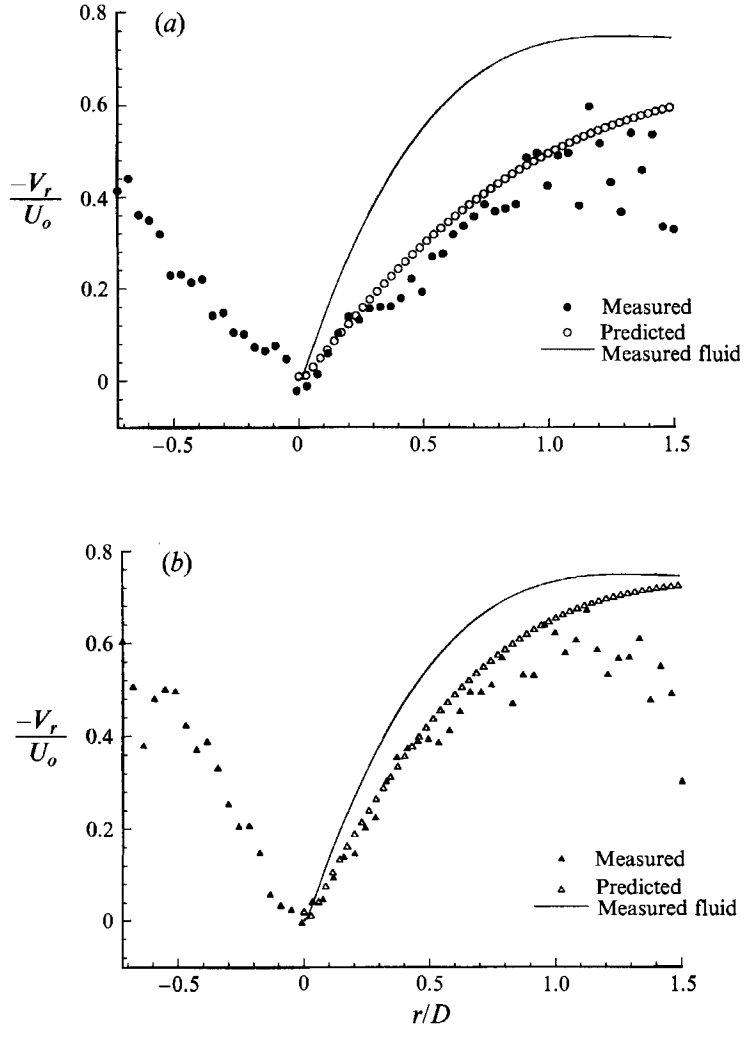

FIGURE 19. Measured and predicted particle radial velocities at $z/D = 0.04$. (*a*) $St_m = 2.4$ and (*b*) $St_m = 0.6$.

the points lie below the calculated velocities. The reason may be that particles, as they move along the plate, lose momentum through interactions with the plate and slower-moving fluid in both the boundary layer and higher z/D planes.

5. Discussion

Our results show that particle rebound is a very important phenomenon in a particle-laden, wall-bounded flow where large normal particle velocities are present. A direct consequence of particle rebound is an abrupt increase in particle number density in the region where rebound trajectories predominate. This phenomenon is largely dependent on the Stokes number associated with the mean flow St_m. For larger St_m, particles became highly concentrated over a large percentage of the stagnation zone. These particles typically possess high axial momentum as they enter the stagnation zone and when they collide with the plate. Since the collisions at

the plate are essentially elastic, no axial momentum is lost, and considerable time is required to slow the particles as they move against the impinging flow. The result is large rebound heights H and significant particle accumulation between the plate and H. Concentration levels and the volume in which the particles accumulate decrease with St_m. In this case, the shorter response time of the particles allows them to decelerate more quickly before and after impact, resulting in lower rebound heights.

Increases in number density can be related directly to the locations in the flow where particles decelerate and residence times lengthen. According to dynamical theory, number density in a steady stream of particles should increase as velocity decreases. Therefore, number density peaks are expected where velocities are minimized. In the case of rebounding particles, this occurs near the apexes of rebound trajectories. The numerical study of Martin & Meiburg (1994) investigating particles in a two-dimensional potential stagnation flow demonstrated this concept. If particles were above a certain Stokes number, then overshoot occurred in the stagnation region. Number densities were largest where particles reversed direction. In Martin & Meiburg's study, a Stokes number of 10 (based on τ_p, ΔU, and δ (the vorticity thickness)) yielded pairs of high-density streaks in the braid regions of a two-dimensional mixing layer. This was thought to occur because of particle overshoot near the free stagnation points there.

The generation mechanism for high particle number density in the present study has some similarities and some differences when compared with that observed in previous work on homogeneous turbulence and free shear layers (e.g. Squires & Eaton 1991; Lazaro & Lasheras 1992; Martin & Meiburg 1994). In the previous work, high particle concentrations were found in regions of high strain rate which persisted over time. The particle motion into these regions was not necessarily aligned with the mean flow direction. Therefore the relative velocity between particles and the straining regions had to be small. In the stagnation flow, however, the straining region is fixed in space, and the particle motion into the regions is aligned with the mean flow. Therefore, a wide range of approach velocities (or St_m) can yield a high-number-density zone. This is because rebounding (analogous to overshoot in Martin & Meiburg's flow) prevents particles from immediately escaping the zone. In the limit of small St_m, particles will simply decelerate to zero at the stagnation point. Assuming Stokes drag, particles approaching the stagnation point in a steady, axisymmetric flow will not overshoot when $St_m < 0.125$. (Refer to Martin & Meiburg 1994 for details of a similar calculation in two-dimensional flow.) As St_m increases, particles rebound and decelerate somewhere above the plate. If multiple rebounds occur in the stagnation zone, then large number densities should be present at more than one height.

The prevailing flow field experienced by the particles in the stagnation zone significantly influences residence times and hence number densities. In order to escape the stagnation zone, the particles must acquire radial velocity somewhere along their trajectories. Rebounding directly affects a particle's ability to acquire radial velocity. For larger St_m, particles rebound to greater heights above the plate where fluid radial velocities (thus drag) are small. Consequently, these particles must 'wait' until they return to the plate, where radial velocities are significant, to be accelerated out of the stagnation zone. For smaller St_m, however, particles remain close to the plate at all times during rebound. Therefore, these particles acquire radial velocity and evacuate the stagnation zone more quickly not only because of their smaller inertia, but also because of the larger radial velocities encountered.

A relationship between particle rebound height and St_m was determined from the

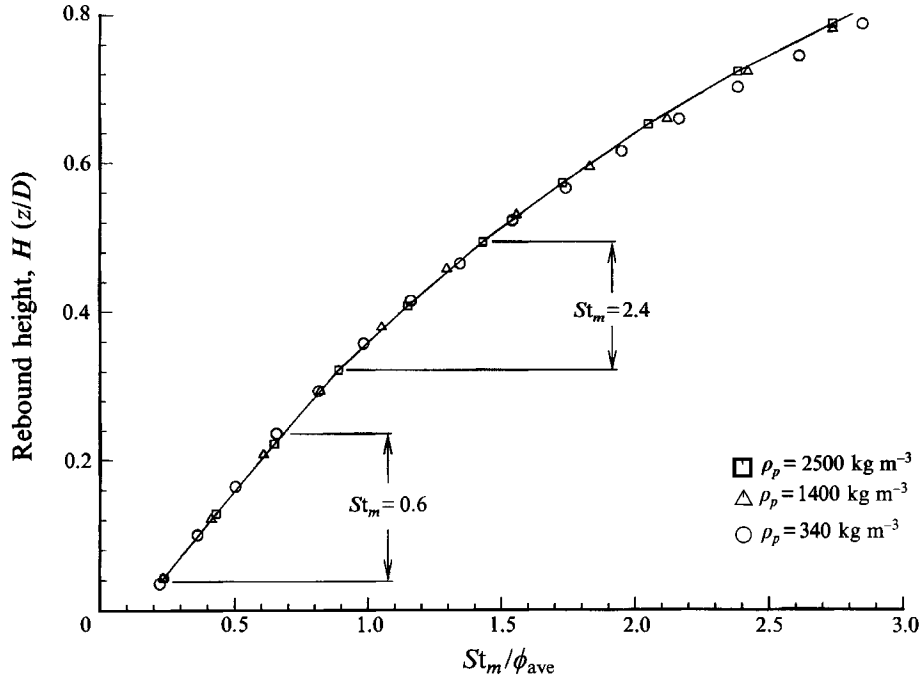

FIGURE 20. Predicted rebound heights versus St_m and average non-Stokesian drag factor ϕ_{ave}. The ranges of calculated rebound heights produced by each group are indicated in the figure.

simplified equation of particle motion along the jet centreline. The results are shown in figure 20. The plot shows that rebound height increases monotonically with St_m as expected and that we are approaching the lower limit of particle rebound for the case of $St_m = 0.6$. The calculated maximum and minimum rebound heights (due to the range of particle diameters) for each particle group are indicated in the figure. The calculated maximum values match fairly well with the maximum rebound height observed in the particle tracking photographs (see figure 6).

More interestingly, figure 20 reveals that St_m is *not* the only parameter on which particle rebound is dependent. Owing to non-Stokesian effects, smaller, denser particles at a given St_m rebound to a larger H compared with larger, less-dense particles. To collapse the data onto a single curve, St_m must be divided by an average non-Stokesian drag factor, ϕ_{ave}:

$$\phi_{\text{ave}} = \frac{1}{N}\sum_{i=1}^{N}\left(1 + 0.15\, Re_{p(i)}^{0.687}\right). \tag{5.1}$$

Values of ϕ are summed over particle trajectories starting immediately after rebound and ending at the rebound height H. This result reveals the importance of non-Stokesian effects in determining flow parameters. An intermediate value of ρ_p is included in the plot to show that the collapse is universal in the range of St_m studied. In the range plotted, ϕ_{ave} varies from 1.2 to greater than 4.

The fluid and particle velocity fields as well as the model analysis above reveal that significant (non-Stokesian) particle Reynolds numbers occur in the stagnation zone. By comparing instantaneous particle velocity fields with the ensemble-averged fluid velocity field, maximum observed slip speeds were 10 m s^{-1} for $St_m = 2.4$ and 6.5 m s^{-1} for $St_m = 0.6$. These slip speeds correspond to Re_p of 16.7 and 14.4

respectively. Maximum Re_p, calculated from the results of the simplified model, were 20 for $St_m = 2.4$ and 11 for $St_m = 0.6$. These Reynolds numbers are high enough to be associated with separation behind spheres in steady flows but not high enough to be associated with vortex shedding. For larger spheres, local acceleration may become strong enough that critical separation and vortex shedding Reynolds numbers are significantly decreased (refer to Magnaudet, Rivero & Fabre 1995). In this case, turbulence modification may be present near the wall even for relatively small mass loadings. The increased local number density due to rebounding and deceleration in these regions would serve to amplify this effect.

The instantaneous number density values and particle distribution in the stagnation zone depend on the influx of particles into this region. When large-scale vortices are present in the free jet, particle concentration levels become spatially non-uniform. Particles accumulate and form clusters in the straining regions between successive vortex rings, where fluid axial velocities decrease and radial velocities increase. Particles immediately downstream of a vortex can be dispersed into, and possibly beyond, the shear layer, while particles in the centre of a ring are accelerated downstream and toward the jet axis. The non-uniformities can intensify as the flow moves downstream, causing particle concentrations entering the stagnation zone to be phase dependent. In addition, the particle history (i.e. impinging or rebounding) that dominates the stagnation zone can also be phase dependent. These effects are integrally related to St'.

For $St' = 1.25$, the overall effect of the vortices was to focus the particles along the jet axis, which was partially due to their initial radial distribution within the flow. There was virtually no particle dispersion across the shear layer. Each particle cluster that formed lost its definition as it approached the plate owing to interactions with the vortex immediately downstream. The cluster eventually reached the centre of this ring and, in doing so, became a highly concentrated mass of particles near the jet axis (refer to figures 7–10, *b* and *d*). Immediately downstream of this cluster, however, particle concentrations were much lower (see figure 7*d*). Consequently, maximum number density values in the stagnation zone varied by up to 30% for this case. In addition, particle distribution and histories were noticeably phase dependent. Particle rebound was very strong immediately after the impingement of the clusters.

For $St' = 0.3$, many particles were dispersed into and across the shear layer in the free jet, and thus these particles never entered the stagnation zone. The clusters that formed between successive vortices were well defined as they approached the plate. In addition, cluster spacing was such that a significant number of particles evacuated the stagnation zone between the impingement of successive clusters. As a result, peak number density values in the stagnation zone were more dependent on phase than in the case of $St' = 1.2$, fluctuating by as much as 50%. Rebounding particles were most dominant above the plate immediately after cluster impingement. Otherwise, impinging particles predominated.

As discussed above, vortices in the flow can produce noticeable effects in the free jet regarding particle distributions and velocities. However, they have much less of an impact in the stagnation zone. As a vortex ring approaches the plate, its induced velocity field in the axial direction is severely damped by the boundary. Radial fluid velocities intensify significantly between the plate and the vortex core, but the effects are local to the ring core only. Hence, the vortices have little effect on fluid velocities (thus particle velocities) in the stagnation zone where particle accumulations are highest. As a result, the motion of most particles near the plate is strictly dependent on St_m, and the observed phase dependence of particle number density is almost exclusively an upstream effect.

The vortex rings do have some effect on the motion of particles near the boundary. Particles moving outward through the shear layer upon impingement are able to remain downstream of and associated with a single vortex ring throughout the flow. The motion of these particles, which never enter the stagnation zone, is strongly affected by the vortices. This occurred for $St' = 0.3$ only. Particles that do enter the stagnation zone downstream of a vortex must rely on the mean flow to transport them into the wall jet. Only particles beyond $r/D \approx 0.4$ feel additional radial drag as vortices impinge upon the plate. Since residence time in the stagnation zone can be significant owing to rebound and deceleration, particles may skip one or more cycles (i.e. vortices) before they can exit the stagnation zone and eventually ride ahead of another vortex. We presume that the number of cycles skipped increases with both St_m and St'.

Since particle distribution varies among the particle groups at the entrance to the stagnation zone, it is difficult to make quantitative comparisons between the number density maps. If the heavier T7 particles were distributed over a wider radius upon exiting the nozzle, they would have had much more interaction with shear layer vortices and been more widely distributed throughout the jet core upon entrance to the stagnation zone. As a result, a broader zone of high concentration would form, but its height should remain the same. Consequently, a more direct interaction between rebounding particles and vortices would emerge. In addition, peak particle concentration levels would most likely decrease for this group since particles would be distributed over a larger cross-sectional volume.

The results presented are based on a fixed nozzle-to-plate spacing which was chosen to achieve small particle slip velocities as the flow entered the stagnation zone. In general, a smaller spacing does not allow particles to accelerate to the jet centreline velocity while a larger spacing results in the fluid centreline velocity decaying faster than particle velocities. These two cases would yield decreased and increased particle rebound heights respectively. Also, a larger spacing would allow more time for particles to interact with the shear layer, further complicating the flow.

Decreasing St' by decreasing the forcing frequency would cause the spatial non-uniformity of particle distributions in the free jet to become more significant. Vortex spacing would increase, and the particle clusters that form would be more discrete. As a result, the influx of particles and resulting stagnation-zone number density levels would be more phase dependent than in the cases described here.

Altering St_m by varying U_o instead of τ_p could have some effects on the mean flow characteristics. For example, the initial particle distribution may be affected by decreasing U_o. In our case, the initial conditions were different for each particle group owing to flow through the contraction. With a smaller U_o, particles with larger τ_p could follow fluid streamlines through the contraction more closely owing to smaller fluid accelerations, thus allowing for more similar initial distributions between the groups. The disadvantage of using a smaller U_o, however, is the increased difficulty involved in generating a steady particle-laden flow exiting the jet nozzle. As U_o is decreased, accumulation of particles in the feed system becomes increasingly troublesome.

6. Summary and conclusions

Results of instantaneous flow visualization studies show that particle rebound is a dominant feature in the stagnation zone of a particle-laden impinging jet for $St_m > 0.6$. Particles cannot follow strongly diverging fluid streamlines nor decelerate with the fluid and, therefore, collide with the plate at large angles of incidence and at high

speed. Collisions with the smooth plate are nearly elastic, and the particles rebound strongly into the impinging flow. Particle number density levels are significantly higher in the stagnation zone than in the free jet immediately upstream. The rebounding, decelerating particles accumulate in the stagnation zone because of long residence times. Maximum rebound height and the height of the region of increased particle concentration are well correlated and increase with the mean Stokes number St_m. In addition, observed rebound heights compare favourably with those predicted by a simplified equation of motion based on drag and gravitational forces. The model revealed that, owing to non-Stokesian effects, particle rebound is a function of both St_m and Re_p. In some locations, Re_p was large enough to indicate separation behind particles.

Particles gain radial velocity near the peaks of their rebound trajectories where their residence times are longest. Fluid radial velocities increase with proximity to the plate. Therefore, radial acceleration of larger particles (associated with larger St_m) is impeded both by their larger inertia and by the smaller fluid radial velocities that they encounter during rebound.

In forced flow, vortices in the free jet produce spatial variations in particle concentration which cause temporal fluctuations in stagnation-zone number density. The influence of vortices (and thus St') on velocities in the stagnation zone is limited to regions close to the shear layer. For $St' > 0.3$, vortices enhance radial drag only when particles enter the shear layer prior to impact or after particles have migrated to $r/D \geqslant 0.4$. In this regime, then, the mean Stokes number St_m is a stronger determinant of particle behaviour in the stagnation zone than St'.

This work is supported by the Electric Power Research Institute under Contract RP 8034-01. We thank the 3M Corporation for generous materials support and Mr Terry Johnson for software development.

REFERENCES

ANDERSON, S. L. 1995 Dynamics of particle motion in an impinging air jet. PhD dissertation, University of Minnesota.

CHEIN, R. & CHUNG, J. N. 1987 Effects of vortex pairing on particle dispersion in turbulent shear flows. *Intl J. Multiphase Flow* **13**, 785–802.

CHUNG, J. N. & TROUTT, T. R. 1988 Simulation of particle dispersion in an axisymmetric jet. *J. Fluid Mech.* **186**, 199–222.

CLIFT, R., GRACE, J. R. & WEBER, M. E. 1978 *Bubbles, Drops, and Particles.* Academic Press.

CROWE, C. T., GORE, R. A. & TROUTT, T. R. 1985 Particle dispersion by coherent structures in free shear flows. *Part. Sci. Technol.* **3**, 149–158.

DIDDEN, N. & HO, C. M. 1985 Unsteady separation in a boundary layer produced by an impinging jet. *J. Fluid Mech.* **160**, 235–256.

GUTMARK, E., WOLFSHTEIN, M. & WYGNANSKI, I. 1978 The plane turbulent impinging jet. *J. Fluid Mech.* **88**, 737–756.

HANSELL, D., KENNEDY, I. M. & KOLLMANN, W. 1992 A simulation of particle dispersion in a turbulent jet. *Intl J. Multiphase Flow* **18**, 559–576.

HISHIDA, K., ANDO, A. & MAEDA, M. 1992 Experiments on particle dispersion in a turbulent mixing layer. *Intl J. Multiphase Flow* **18**, 181–194.

ISHIMA, T., HISHIDA, K. & MAEDA, M. 1993 Effect of particle residence time on particle dispersion in a plane mixing layer. *Trans. ASME* I: *J. Fluids Engng* **115**, 751–759.

KAMALU, N., TANG, L., TROUTT, T. R., CHUNG, J. N. & CROWE, C. T. 1989 Particle dispersion in developing shear layers. *Intl Conf. on Mechanics of Two-Phase Flows, Taipei*, pp. 199–202.

KAMALU, N., WEN, F., TROUTT, T. R., CROWE, C. T. & CHUNG J. N. 1988 Particle dispersion by ordered motion in turbulent mixing layers. *ASME Forum on Cavitation and Multiphase Flow*, pp. 150–154.

KUROSAKI, Y., MURASAKI, T., SATOH, I. & KASHIWAGI, T. 1986 Study on heat transfer mechanism of a gas-solid suspension impinging jet. *Heat Transfer* **5**, 2587–2592.

LANDRETH, C. C. & ADRIAN, R. J. 1990 Impingement of a low Reynolds number turbulent circular jet onto a flat plate at normal incidence. *Exps. Fluids* **9**, 79–84.

LAZARO, B. J. & LASHERAS, J. C. 1989 Particle dispersion in a turbulent plane shear layer. *Phys. Fluids* A **1**, 1035–1044.

LAZARO, B. J. & LASHERAS, J. C. 1992*a* Particle dispersion in the developing free shear layer. Part 1. Unforced flow. *J. Fluid Mech.* **235**, 143–178.

LAZARO, B. J. & LASHERAS, J. C. 1992*b* Particle dispersion in the developing free shear layer. Part 2. Forced flow. *J. Fluid Mech.* **235**, 179–221.

LONGMIRE, E. K. & EATON, J. K. 1992 Structure of a particle-laden round jet. *J. Fluid Mech.* **236**, 217–257.

LONGMIRE, E. K. & EATON, J. K. 1994 Active open-loop control of particle dispersion in round jets. *AIAA J.* **32**, 555–563.

MAGNAUDET, J., RIVERO, M. & FABRE, J. 1995 Accelerated flows past a rigid sphere or a spherical bubble. *J. Fluid Mech.* **284**, 97–136.

MARTIN, J. E. & MEIBURG, E. 1994 The accumulation and dispersion of heavy particles in forced two-dimensional mixing layers. Part I: The fundamental and subharmonic cases. *Phys. Fluids* **6**, 1116–1132.

MAXEY, M. R. 1987 The gravitational settling of aerosol particles in homogeneous turbulence and random flow fields. *J. Fluid Mech.* **174**, 441–465.

PEDINOTTI, S., MARIOTTI, G. & BANERJEE, S. 1992 Direct numerical simulation of particle behaviour in the wall region of turbulent flows in horizontal channels. *Intl J. Multiphase Flow* **18**, 927–941.

RASHIDI, M., HETSRONI, G. & BANERJEE, S. 1990 Particle-turbulence interaction in a boundary layer. *Intl J. Multiphase Flow* **16**, 935–949.

SHIMIZU, A., ECHIGO, R. & HASEGAWA, S. 1979 Impinging jet heat transfer of gas-solid suspension medium. *Advances in Enhanced Heat Transfer, Proc. 18th National Heat Transfer Conf., San Diego, California*, pp. 155–160.

SQUIRES, K. D. & EATON, J. K. 1991 Preferential concentration of particles by turbulence. *Phys. Fluids* A **3**, 1169–1178.

WANG, L. P. & MAXEY, M. R. 1993 Settling velocity and concentration distribution of heavy particles in homogeneous isotropic turbulence. *J. Fluid Mech.* **256**, 27–68.

WEN, F., KAMALU, N., CHUNG, J. N., CROWE, C. T. & TROUTT, T. R. 1992 Particle dispersion by vortex structures in plane mixing layers. *Trans. ASME* I: *J. Fluids Engng* **114**, 657–666.

YOSHIDA, H., SUENAGA, K. & ECHIGO, R. 1990 Turbulence structure and heat transfer of a two-dimensional impinging jet with gas-solid suspensions. *Intl J. Heat Transfer* **33**, 859–867.